

Generate in Reconstruction Space, Match in Semantic Space: Transport Geometry for One-Step Generation

Hugues Van Assel Edward De Brouwer Saeed Saremi
Gabriele Scalia Aviv Regev
Genentech

Abstract

Generative modeling and self-supervised representation learning (SSL) optimize structurally different objectives: generative training rewards distributional fidelity, while SSL rewards semantic coherence. Yet recent work repeatedly finds that SSL features improve generative training, though the mechanism of this synergy remains unclear. Here, we study the benefits of SSL in generative modeling in the framework of one-step generation where the role of representation is explicit: frozen SSL features are used to match generated samples to real data. We use the Sinkhorn divergence in that feature space, providing a tractable surrogate for the Wasserstein distance, the population-level discrepancy approximated by Fréchet-style evaluation metrics (such as FID). We find that this objective becomes highly effective when computed in a semantically structured SSL feature space (a $39\times$ reduction in ImageNet FID). We trace this behavior primarily to matching estimation: semantic SSL features that suppress nuisance reconstruction details induce a more compact geometry, making distribution matching more tractable. As a consequence, the best training SSL features need not match the features used by the evaluation metric. In particular, we show that using Inception as the feature extractor can improve FID while degrading matching stability and sample quality, revealing a form of metric hacking. Using extensive experiments on ImageNet, we identify which SSL feature families lead to best generation performance and show that matching stability is a quantitative criterion for selecting them. Code is available at <https://github.com/Genentech/semantic-transport-generation>.

1 Introduction

Self-supervised representation learning and generative modeling have matured as two central yet historically separate paradigms in AI. Generative modeling aims to learn a data distribution well enough to synthesize new samples: from latent-variable one-step mappings (e.g., VAEs, GANs, normalizing flows) to iterative noise-to-data trajectories in diffusion, score-based, and flow-matching families [22, 15, 9, 20, 38, 26, 27]. In this paradigm, success is judged by synthesis quality and coverage, because the downstream goal is generation itself. Self-supervised learning targets a different objective: learning representations that expose semantic structure and invariances useful for downstream perception tasks. Methods range from reconstruction-style objectives (e.g., masked autoencoding) to latent alignment and joint-embedding objectives (e.g., contrastive or self-distillation families) [18, 17, 16, 30, 40]. Here, success is measured by downstream transfer rather than sample synthesis: representations are evaluated either frozen (e.g., linear probe or k-NN) or after end-to-end fine-tuning on tasks such as classification, detection, segmentation, depth, and robustness.

These objectives are formally orthogonal, yet there is growing empirical evidence that aligning generative training with pretrained SSL representations improves performance at multiple levels of the generative pipeline [45, 44, 46]. Depending on the method, the SSL feature extractor serves as a regularizer [45, 43, 42, 37], an alignment target [44, 24, 6, 5], or a generative substrate [46, 12, 23]. Yet why it helps in each case remains poorly understood.

To study this question we focus on one-step generative models trained by distribution matching, in which a generator maps noise directly to data by minimizing a discrepancy between generated and real samples. Early work formulated this matching in the ambient data space [3, 11, 25]. However, these methods have historically been difficult to scale and have generally fallen short of the strongest generative models [14, 25]. In this work, we lift the distributional matching objective to a feature space. Unlike approaches that use the feature extractor as an auxiliary regularizer, here it plays a first-order role: it directly defines the geometry in which generated and real samples are compared, and therefore shapes the training signal. This choice also creates a structural alignment with standard evaluation: Fréchet-style metrics are Gaussian approximations to Wasserstein-type discrepancies in feature space, so training and evaluation measure the same quantity up to the choice of extractor. One-step generation in this framework is therefore an unusually transparent setting for studying what makes a feature extractor effective for generative training.

Contributions. Our approach is motivated by the intuition that **semantically rich feature spaces are geometrically better suited to distribution matching than reconstruction-oriented spaces**. By discarding nuisance reconstruction variation and concentrating on semantic variation, these features yield a lower-dimensional problem with better statistical properties. At a high level, our approach breaks down the challenging problem of learning to sample from a high-dimensional data distribution into two stages (Figure 1): we generate samples in an auto-encoding reconstruction space, but set up the distributional matching objective in a semantic space built on top of it, which by design has a better geometry (Figure 2). This separation of generation and matching into two spaces with distinct geometric roles is the core conceptual idea of this work. Our contributions are as follows:

- **Semantic features unlock competitive one-step generation.** We perform matching in a frozen SSL feature space using the Sinkhorn divergence, a discrepancy that interpolates between Wasserstein distance and MMD, while generating in the reconstruction-oriented latent space of a pretrained VAE (Figure 1). One-step Sinkhorn-based generation without a semantic feature extractor is severely limited [14]; we show that SSL features built directly in the reconstruction latent space reduce FID-Inception by $39\times$ on class-conditional ImageNet (Table 1), closing much of the gap to multi-step diffusion and flow-matching models for a generator trained from scratch, via a classifier-free guidance formulation for Sinkhorn training (Section 3.2). We provide precise recipes for obtaining such features, either by training SSL models directly on VAE latents (Section C.2.1) or by distilling pretrained SSL models such as DINOv3 into the VAE latent space (Section C.2.2), and compare both approaches in Section 4.2.
- **Matching-estimation stability as a key criterion.** The dramatic improvement raises the question of what makes an SSL feature extractor effective in this framework. We identify transport estimation quality as the primary driver: features with lower intrinsic dimensionality induce more stable OT transport plans within the Sinkhorn divergence and more reliable training signals (Figure 2). We derive the OT stability metric \tilde{D}_N (Section 4.1), which directly predicts generation quality across extractor families (Table 1) and provides a computation-light selection criterion without full training runs. As a direct consequence, the optimal training feature extractor does not always match the evaluation feature extractor: geometric alignment with the evaluation metric and OT estimation stability are two distinct criteria that can point to different extractors, and optimizing for the former alone can hurt training (Section 3.1).
- **Evaluation geometry exposes metric limitations.** When the training feature extractor coincides with the evaluation feature extractor, Sinkhorn training optimizes a discrepancy structurally aligned with the evaluation metric, enabling a form of metric hacking. In particular, using Inception as the training feature extractor directly targets the same feature space as FID, yielding competitive Fréchet scores while producing perceptually inferior samples (Figure 4, Table 1). Beyond our specific framework, this highlights a broader weakness of widely used feature-based metrics in generative modeling: strong performance on FID does not imply better sample quality.

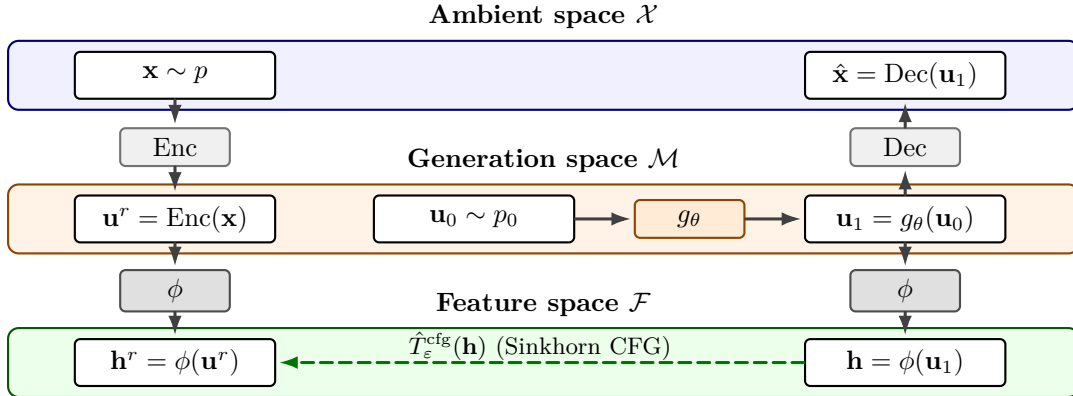


Figure 1: Overview. A prior state $\mathbf{u}_0 \sim p_0$ is mapped in one step by g_θ to a generated state \mathbf{u}_1 in generation space \mathcal{M} , then decoded to the ambient sample $\hat{\mathbf{x}} = \text{Dec}(\mathbf{u}_1)$. In parallel, a real datum $\mathbf{x} \sim p$ is encoded into the generation-space target $\mathbf{u}^r = \text{Enc}(\mathbf{x})$. Both states are embedded by the frozen SSL feature extractor ϕ into feature vectors $\mathbf{h} = \phi(\mathbf{u}_1)$ and $\mathbf{h}^r = \phi(\mathbf{u}^r)$, and the training loss is a Sinkhorn transport problem in feature space \mathcal{F} . Thus, generation is performed in generation space, while the transport geometry used for training is defined in feature space. In practice, the loss is evaluated over minibatches; the figure shows the same construction schematically for a single pair of states. In input-space models, $\mathcal{M} = \mathcal{X}$ and $\text{Enc} = \text{Dec} = \text{Id}$. In latent-space models, applying ϕ directly on the compact generation space \mathcal{M} (e.g., a VAE latent) avoids decoding to pixels; in our experiments, ϕ is obtained by training from scratch or distilling ambient feature extractors (DINOv3, Inception) into generation space.

2 Background

This section introduces the background material for this work. We start with optimal transport and the Sinkhorn divergence, which formalize distribution matching in feature space and provide our practical training objective. We also cover prior work on statistical estimation of OT maps from finite samples [33]. We close with an overview of prior works leveraging SSL representations in generative models.

Entropic OT and Sinkhorn divergence. We leverage optimal transport to compare generated and target distributions in the feature space where the cost is defined. For probability measures $P, Q \in \mathcal{P}_2(\mathcal{F})$ on a feature space \mathcal{F} , the quadratic transport objective is

$$W_2^2(P, Q) := \min_{\pi \in \Pi(P, Q)} \int_{\mathcal{F} \times \mathcal{F}} \|\mathbf{h} - \mathbf{h}'\|^2 d\pi(\mathbf{h}, \mathbf{h}'). \quad (1)$$

Here $\Pi(P, Q)$ denotes the set of couplings between P and Q . W_2 is a proper metric on the space of probability measures: unlike likelihood-based divergences, it remains finite and provides a useful training signal even when generated and real distributions have disjoint support, making it a natural population-level objective for generative modeling [41, 3, 14]. Given generic empirical measures $\alpha = \frac{1}{N} \sum_{i=1}^N \delta_{\mathbf{h}_i}$ and $\beta = \frac{1}{N} \sum_{j=1}^N \delta_{\mathbf{h}'_j}$ on \mathcal{F} , entropic regularization provides a tractable finite-sample approximation to the quadratic Wasserstein problem: it smooths the coupling problem with an entropy penalty, is computable by Sinkhorn iterations, and is well suited to parallel GPU implementation [7, 32]:

$$\text{OT}_\varepsilon(\alpha, \beta) = \min_{\pi \in \Pi(\alpha, \beta)} \sum_{i,j} \pi_{ij} C_{ij} + \varepsilon \sum_{i,j} \pi_{ij} \log \pi_{ij}, \quad (2)$$

where $C_{ij} = \|\mathbf{h}_i - \mathbf{h}'_j\|^2$ and $\Pi(\alpha, \beta)$ is the set of coupling matrices with marginals α and β . However, $\text{OT}_\varepsilon(\alpha, \alpha) > 0$ even when both arguments coincide, causing entropic bias and shrinkage when used

as a training loss. The *Sinkhorn divergence* [14, 11] removes this bias:

$$S_\varepsilon(\alpha, \beta) = \text{OT}_\varepsilon(\alpha, \beta) - \frac{1}{2} \text{OT}_\varepsilon(\alpha, \alpha) - \frac{1}{2} \text{OT}_\varepsilon(\beta, \beta). \quad (3)$$

It satisfies $S_\varepsilon(\alpha, \alpha) = 0$, metrizes weak convergence, and interpolates between unregularized OT and MMD [11]. In our setting, Sinkhorn is therefore the practical surrogate to the ideal quadratic Wasserstein objective.

Matching estimation. In practice, the Sinkhorn divergence is computed over finite mini-batches rather than the full distributions. From each mini-batch, the Sinkhorn solver produces a coupling π (see Section B) that assigns to each generated feature \mathbf{h}_i a target indicating where it should move to better match the real distribution; this per-point target is the matching signal that drives generator training. A key question is then how faithfully this finite-sample signal tracks the ideal population-level matching map: poor estimation quality translates directly into noisy and unreliable training gradients, regardless of the quality of the Sinkhorn objective itself. The *entropic barycentric estimator* maps each source point to its barycenter under the optimal coupling π : $\hat{T}_\varepsilon(\mathbf{h}_i) = N \sum_{j=1}^N \pi_{ij} \mathbf{h}'_j$. Under regularity assumptions on the feature marginals, this estimator converges to the ideal population Monge map T_0 , the unique map $T_0: \mathcal{F} \rightarrow \mathcal{F}$ pushing P forward to Q minimizing $\mathbb{E}_P[\|T_0(\mathbf{h}) - \mathbf{h}\|^2]$ (Brenier’s theorem) [33], with mean-squared estimation error (in L^2 under the source population measure) decaying as

$$\mathbb{E}\|\hat{T}_\varepsilon - T_0\|_{L^2}^2 \lesssim N^{-\frac{s+2}{2(d+s+2)}} \log N, \quad (4)$$

where d is the intrinsic dimensionality of the feature distribution and $s \leq 2$ the Hölder smoothness of the source and target feature densities. The rate is controlled primarily by d : more compact feature distributions yield faster estimation and more reliable matching signals from finite minibatches. This is the statistical bridge we use later: selecting SSL feature extractors that reduce d directly improves matching estimation quality.

SSL for generation. There is growing empirical evidence that aligning generative training with pretrained SSL representations improves performance across multiple levels of the generative pipeline. At the generator level, REPA [45] shows clear optimization gains by regularizing the denoiser’s intermediate representations to align with clean features from a frozen pretrained visual featurizer; follow-up work refines the alignment schedule [43], proposes dispersive representation regularization [42], and probes which SSL featurizer properties drive alignment gains [37]. At the encoder level, recent work aligns or redesigns latent spaces using foundation representations, including end-to-end tuning and alignment of autoencoders [44, 24, 6, 5]. Beyond regularization and encoder alignment, some approaches use SSL representations as a generative substrate, generating directly in an SSL feature space [46, 12, 23]; these require learning a decoder from that space back to the pixel domain, which is a non-trivial additional task. Among prior work, the drifting approach [8] is most closely related to ours: it also performs one-step generation and leverages SSL features, but approximates the transport cost via a one-round double-softmax rather than solving a proper matching problem. Grounding the matching cost in the Sinkhorn divergence allows direct application of the matching estimation theory above [33], enabling a more transparent study of the SSL featurizer’s effect on generation quality; see Section F for a detailed comparison with drifting. Across all these approaches, why SSL features help generation remains poorly understood: the gains are empirical, and it is unclear which properties of the representations drive the performance gains.

3 Feature Geometry for One-Step Generation

This section formalizes one-step generation in a feature space defined by a frozen SSL extractor (Figure 1). Section 3.1 introduces the generation setup and studies the gap between the training and evaluation objectives, identifying two key featurizer-dependent quantities: geometric alignment with the evaluation featurizer, and matching estimation quality from finite minibatches. Section 3.2 then derives the Sinkhorn training objective with classifier-free guidance.

3.1 Feature Geometry and Training-Evaluation Gap

Generation space. Let \mathcal{X} denote the ambient data space and p the data distribution on \mathcal{X} . Generation is performed in a *generation space* \mathcal{M} , whose primary characteristic is that it admits mappings to and from the ambient space, namely an encoder $\text{Enc} : \mathcal{X} \rightarrow \mathcal{M}$ and decoder $\text{Dec} : \mathcal{M} \rightarrow \mathcal{X}$. Following latent diffusion [35], \mathcal{M} is typically a compact latent space (e.g. a VAE latent) so that generation is more tractable than in \mathcal{X} directly. We perform generation by sampling prior samples $\mathbf{u}_0 \in \mathcal{M}$ from a noise distribution p_0 (typically standard Gaussian) and mapping them with a learnable one-step generator $g_\theta : \mathcal{M} \rightarrow \mathcal{M}$. These samples are then decoded to ambient space with the decoder. The one-step generator g_θ is trained by matching generated points $g_\theta(\mathbf{u}_0)$ to real data points $\mathbf{x} \sim p$ encoded with $\mathbf{u}^r := \text{Enc}(\mathbf{x}) \in \mathcal{M}$.

Matching cost in Feature space. The defining choice of our approach is to measure the discrepancy between generated and real samples not in \mathcal{M} or \mathcal{X} , but in a separate *feature space* \mathcal{F} with different geometric properties, designed to be more suitable for matching estimation. Concretely, a frozen SSL feature extractor $\phi : \mathcal{M} \rightarrow \mathcal{F}$ is applied directly to points in generation space, avoiding a round-trip through the decoder to ambient space and keeping feature extraction computationally efficient. The transport cost is the squared feature distance $\|\phi(\mathbf{u}) - \phi(\mathbf{u}')\|^2$. The featurizer ϕ therefore determines both the population matching geometry and the discrete Sinkhorn problems used to approximate it in practice. We denote $\phi_\star : \mathcal{M} \rightarrow \mathcal{F}_\star$ as the evaluation featurizer defining the evaluation geometry of interest.

Wasserstein objectives. For a generator $g : \mathcal{M} \rightarrow \mathcal{M}$, we define the generated and real feature probability measures

$$q_{\phi,g} := (\phi \circ g)_\# p_0, \quad r_\phi := (\phi \circ \text{Enc})_\# p, \quad (5)$$

and their corresponding evaluation-space feature probability measures

$$q_{\star,g} := (\phi_\star \circ g)_\# p_0, \quad r_\star := (\phi_\star \circ \text{Enc})_\# p. \quad (6)$$

Matching generated and real probability measures in each case corresponds to the following Wasserstein objectives (see Section 2)

$$J_\phi(g) := W_2^2(q_{\phi,g}, r_\phi), \quad J_\star(g) := W_2^2(q_{\star,g}, r_\star). \quad (7)$$

J_ϕ is the population-level training objective, optimized in the geometry of ϕ ; J_\star is the evaluation objective, measuring discrepancy in the geometry of ϕ_\star . The central question is how well minimizing J_ϕ via its empirical Sinkhorn approximation drives J_\star toward zero.

Empirical Sinkhorn objective. Given minibatch samples $\mathbf{u}_{0,1}, \dots, \mathbf{u}_{0,N} \sim p_0$ and $\mathbf{x}_1, \dots, \mathbf{x}_N \sim p$, define the empirical feature measures $\hat{q}_{\phi,g} := \frac{1}{N} \sum_{i=1}^N \delta_{\phi(g(\mathbf{u}_{0,i}))}$ and $\hat{r}_\phi := \frac{1}{N} \sum_{j=1}^N \delta_{\phi(\text{Enc}(\mathbf{x}_j))}$, and the practical one-batch empirical Sinkhorn objective optimized in training:

$$\hat{J}_{\phi,\varepsilon,N}(g) := S_\varepsilon(\hat{q}_{\phi,g}, \hat{r}_\phi). \quad (8)$$

Since J_ϕ is not directly accessible, we train with its empirical Sinkhorn approximation $\hat{J}_{\phi,\varepsilon,N}$. The gap between the evaluation objective and this practical surrogate decomposes into two terms:

$$\Delta_\phi^{\text{geom}}(g) := |J_\star(g) - J_\phi(g)| \quad (\text{geometric misalignment}), \quad (9)$$

$$\Delta_{\phi,\varepsilon,N}^{\text{est}}(g) := |J_\phi(g) - \hat{J}_{\phi,\varepsilon,N}(g)| \quad (\text{matching estimation}). \quad (10)$$

For any generator g , adding and subtracting $J_\phi(g)$ and applying the triangle inequality yields the following upper bound:

Evaluation-Training Gap

$$J_{\star}(g) \leq \hat{J}_{\phi,\varepsilon,N}(g) + \Delta_{\phi}^{\text{geom}}(g) + \Delta_{\phi,\varepsilon,N}^{\text{est}}(g). \quad (11)$$

In particular, the evaluation performance of the learned generator g_{θ} is controlled by its training loss and two residual terms that this work focuses on: the geometric misalignment $\Delta_{\phi}^{\text{geom}}$ between training and evaluation feature spaces, and the matching estimation gap Δ^{est} between the empirical Sinkhorn objective and the population Wasserstein target. Note that the training loss $\hat{J}_{\phi,\varepsilon,N}(g_{\theta})$ itself also depends on ϕ through the smoothness of the feature geometry, which affects how easily the generator can minimize it, an effect we do not quantify explicitly but leave to future work.

Geometric misalignment. The term $\Delta_{\phi}^{\text{geom}}$ measures whether the feature geometry induced by ϕ preserves the semantic matching problem induced by the evaluation encoder ϕ_{\star} . A small value means that improving the training objective also improves the evaluation objective, so this axis captures semantic faithfulness. In the experiments, we operationalize this axis through encoder–evaluation alignment values; see Figure 3. In the ideal case, if $\phi_{\star} = A \circ \phi$ on the relevant supports for some isometric embedding $A : \mathcal{F} \rightarrow \mathcal{F}_{\star}$, then the two encoders induce the same matching geometry up to a distance-preserving change of coordinates. Hence $J_{\star}(g) = J_{\phi}(g)$ for any generator g , and in particular $\Delta_{\phi}^{\text{geom}}(g_{\theta}) = 0$.

Matching estimation. The term Δ^{est} measures whether the practical entropic minibatch training signal under ϕ tracks the ideal quadratic Wasserstein transport problem. The training algorithm accesses this gap through the particle gradient of the empirical Sinkhorn surrogate. For a fixed generator g_{θ} and a minibatch $\{(\mathbf{u}_{0,i}, \mathbf{x}_i)\}_{i=1}^N$, let $\mathbf{h}_i = \phi(g_{\theta}(\mathbf{u}_{0,i}))$ and $\mathbf{h}_j^r = \phi(\text{Enc}(\mathbf{x}_j))$. Then

$$\nabla_{\mathbf{h}_i} \hat{J}_{\phi,\varepsilon,N}(g_{\theta}) = -\frac{2}{N} \left(\hat{T}_{\varepsilon}^{q,r}(\mathbf{h}_i) - \hat{T}_{\varepsilon}^{q,q}(\mathbf{h}_i) \right), \quad (12)$$

where $\pi^{q,r}$ and $\pi^{q,q}$ are the optimal couplings of $\text{OT}_{\varepsilon}(\hat{q}_{\phi,g_{\theta}}, \hat{r}_{\phi})$ and $\text{OT}_{\varepsilon}(\hat{q}_{\phi,g_{\theta}}, \hat{q}_{\phi,g_{\theta}})$ respectively, and $\hat{T}_{\varepsilon}^{q,r}(\mathbf{h}_i) := N \sum_j \pi_{ij}^{q,r} \mathbf{h}_j^r$, $\hat{T}_{\varepsilon}^{q,q}(\mathbf{h}_i) := N \sum_k \pi_{ik}^{q,q} \mathbf{h}_k$ are the corresponding cross- and self-barycentric projections (see Section B for the log-domain algorithms used to compute these). Thus, the empirical Sinkhorn update direction is exactly the cross barycentric map minus the self-transport correction. Under regularity assumptions on the feature marginals, the empirical cross barycentric map converges to the population quadratic-cost Monge map [33] at a rate governed by the intrinsic dimensionality d of the feature distribution (proxied in practice by the effective rank of the feature covariance; see Section 4.2). This makes minibatch target stability a natural observable proxy for matching estimation: if the empirical barycentric targets vary strongly across target subsamples, then the practical Sinkhorn updates are not yet tracking a stable approximation to the ideal Wasserstein transport problem (see \tilde{D}_N , equation 16).

3.2 Sinkhorn Training with Classifier-Free Guidance

We train g_{θ} for class-conditional generation by minimizing the Sinkhorn divergence between generated and real feature distributions in SSL feature space. Write $q_{\phi,\theta}(\cdot|c,w) := (\phi \circ g_{\theta}(\cdot|c,w))_{\#} p_0$ for the generated feature distribution at class label c and guidance weight w , $r_{\phi}^c := (\phi \circ \text{Enc})_{\#} p(\cdot|c)$ for the class-conditional real feature distribution, and $r_{\phi}^u := (\phi \circ \text{Enc})_{\#} p$ for the class-marginal (unconditional) real feature distribution; their minibatch empirical counterparts are $\hat{q}_{\phi,\theta}(\cdot|c,w)$, \hat{r}_{ϕ}^c , \hat{r}_{ϕ}^u . In contrast to standard diffusion CFG, which is applied at inference by mixing conditional and unconditional predictions at the same latent state, we incorporate guidance directly into training by keeping the generated distribution fixed and interpolating between Sinkhorn objectives toward the conditional and unconditional real distributions:

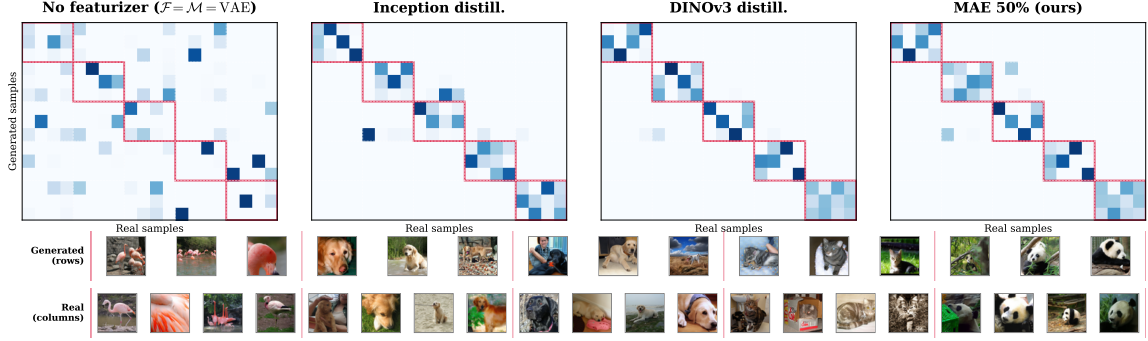


Figure 2: Sinkhorn coupling matrices π^ε between generated samples (rows) and real samples (columns) for five ImageNet classes, including a confusable pair (golden retriever, Labrador). Generated samples are fixed across all panels (from the MAE 50% model); only the featurizer ϕ varies, defining the transport cost $C_{ij} = \|\phi(\mathbf{u}_i) - \phi(\mathbf{u}_j^+)\|^2$. Red outlines indicate the expected same-class blocks along the diagonal. Without a semantic featurizer (left), VAE features alone fail to recover the block-diagonal structure. Inception distillation partially recovers the block-diagonal structure, while DINOv3 distillation and MAE 50% produce sharper same-class matching. Coupling computed with $\varepsilon = 0.05 \cdot \text{std}(C)$ and 50 Sinkhorn iterations.

Sinkhorn CFG Training Objective

$$\min_{\theta} (1+w) S_\varepsilon(\hat{q}_{\phi,\theta}(\cdot|c,w), \hat{r}_\phi^c) - w S_\varepsilon(\hat{q}_{\phi,\theta}(\cdot|c,w), \hat{r}_\phi^u) \quad (13)$$

where $w \geq 0$ is the guidance weight. Since the envelope theorem fixes the Sinkhorn couplings at their optimal values, no backpropagation through the solver is required, and the gradient of the minimized objective with respect to the generated features is $-\frac{2}{N} \hat{T}_\varepsilon^{\text{cfg}}(\mathbf{h}_i)$, where

$$\hat{T}_\varepsilon^{\text{cfg}}(\mathbf{h}_i) = (1+w) \hat{T}_\varepsilon^{q,c}(\mathbf{h}_i) - w \hat{T}_\varepsilon^{q,u}(\mathbf{h}_i) - \hat{T}_\varepsilon^{q,q}(\mathbf{h}_i), \quad (14)$$

and $\hat{T}_\varepsilon^{q,c}(\mathbf{h}_i)$, $\hat{T}_\varepsilon^{q,u}(\mathbf{h}_i)$ are the conditional and class-marginal cross-transport barycenters, mirroring the standard CFG decomposition: the first term amplifies the conditional signal and the second subtracts the class-agnostic one, with strength w . Three Sinkhorn solves are needed per step: conditional cross, class-marginal cross, and self-transport; since both divergences share the same generated distribution, their self-transport terms coincide and contribute a single $\hat{T}_\varepsilon^{q,q}$ term. At inference, choose a class label c and guidance weight w , sample $\mathbf{u}_0 \sim p_0$, map $\mathbf{u}_1 = g_\theta(\mathbf{u}_0 | c, w)$, and decode $\hat{\mathbf{x}} = \text{Dec}(\mathbf{u}_1)$.

4 Experiments

We study class-conditional generation varying the frozen SSL feature extractor ϕ , measuring generation quality and featurizer diagnostics with the metrics below. The main experiments cover ImageNet image generation; experiments with single-cell RNA-Seq can be found in Section E.

4.1 Evaluation metrics

Fréchet metrics. The standard quality metric in generative modeling, across both natural images [19] and single-cell genomics, is the Fréchet distance in the feature space \mathcal{F}_* of a fixed evaluation featurizer ϕ_* . Writing $\boldsymbol{\mu}_r, \boldsymbol{\Sigma}_r$ and $\boldsymbol{\mu}_f, \boldsymbol{\Sigma}_f$ for the mean and covariance of r_* and q_{*,g_θ} respectively,

$$\text{FD}_{\phi_*} = \|\boldsymbol{\mu}_r - \boldsymbol{\mu}_f\|^2 + \text{tr}\left(\boldsymbol{\Sigma}_r + \boldsymbol{\Sigma}_f - 2\left(\boldsymbol{\Sigma}_r^{1/2}\boldsymbol{\Sigma}_f\boldsymbol{\Sigma}_r^{1/2}\right)^{1/2}\right), \quad (15)$$

Table 1: Unified featurizer comparison on ImageNet class-conditional generation (default backbone: 32-layer ViT). All results are from our method (Section 3.2). Metrics as defined in Section 4.1. **Bold**: best per column; underline: second best.

Featurizer	FID-Inc↓	FD-DINOv3↓	FD-VAE↓	Eff. rank	\tilde{D}_{128} ↓
No featurizer ($\mathcal{M} = \mathcal{F}$)	134.56	90.45	179.80	79.0	0.194
Inception distill.	4.88	68.84	510.26	87.0	0.240
DINOv3 distill.	<u>3.60</u>	<u>43.87</u>	<u>129.31</u>	68.0	0.191
MAE (mask 75%)	6.66	40.87	161.38	57.3	0.170
MAE (mask 60%)	3.84	59.05	149.60	50.0	<u>0.168</u>
MAE (mask 50%)	3.46	57.48	127.34	52.1	0.164

which equals $W_2^2(\mathcal{N}(\boldsymbol{\mu}_r, \boldsymbol{\Sigma}_r), \mathcal{N}(\boldsymbol{\mu}_f, \boldsymbol{\Sigma}_f))$ [10], a lower bound on $W_2^2(r_*, q_{*,g_\theta}) = J_*(g_\theta)$ [13]; hence $\text{FD}_{\phi_*} \leq J_*(g_\theta)$, a computable lower bound on the evaluation objective in equation 11. We report FD_{ϕ_*} for multiple evaluation featurizers, probing featurizer–metric alignment across feature spaces.

OT matching estimation stability. We measure the normalized barycentric disagreement

$$\tilde{D}_N := \frac{1}{C_\phi} \cdot \frac{1}{N} \sum_{i=1}^N \|\hat{T}_{\varepsilon, \mathcal{A}}^{q,r}(\mathbf{h}_i) - \hat{T}_{\varepsilon, \mathcal{B}}^{q,r}(\mathbf{h}_i)\|^2, \quad (16)$$

where \mathcal{A}, \mathcal{B} are two independent size- N draws from a held-out target pool (mimicking two different training minibatches), $\hat{T}_{\varepsilon, \mathcal{A}}^{q,r}(\mathbf{h}_i) = N \sum_{j \in \mathcal{A}} \pi_{ij}^\varepsilon \mathbf{h}_j^r$ is the resulting Sinkhorn cross-transport barycentric map, and C_ϕ is the empirical variance of target features, making \tilde{D}_N scale-invariant across featurizer families. A small \tilde{D}_N means empirical transport targets are stable across minibatch resamples; a large value indicates erratic training directions and a larger matching estimation gap.

Effective rank. The effective rank $\exp(-\sum_i \bar{\lambda}_i \log \bar{\lambda}_i)$, where $\bar{\lambda}_i := \lambda_i / \sum_j \lambda_j$ and $\{\lambda_i\}$ are the eigenvalues of the target feature covariance, proxies the intrinsic dimensionality of the feature distribution; by the estimation rate in equation 4 [33], lower intrinsic dimensionality implies faster OT map estimation.

4.2 Setup

We study class-conditional generation on ImageNet at 256×256 resolution. Following latent diffusion [35], generation is performed in the latent generation space $\mathcal{M} \cong \mathbb{R}^{4 \times 32 \times 32}$ of the frozen Stable Diffusion VAE [35]:¹ the encoder $\text{Enc} : \mathcal{X} \rightarrow \mathcal{M}$ maps real images to latent targets $\mathbf{u}^r = \text{Enc}(\mathbf{x})$ for $\mathbf{x} \sim p$, and the decoder $\text{Dec} : \mathcal{M} \rightarrow \mathcal{X}$ maps generated latents back to pixels. The generator g_θ is DriftDiT-B/2 [31]: a DiT-Base transformer with patch size 2 operating on 32×32 latents. We train with AdamW (lr = 4×10^{-4}), using $(N_{\text{pos}}, N_{\text{neg}}, N_{\text{unc}}) = (128, 64, 32)$ positive, generated/self, and unconditional samples per class, and a cosine schedule over 400k steps on 8 GPUs. We evaluate with three instances of FD_{ϕ_*} (Eq. 15), each corresponding to a different evaluation featurizer ϕ_* applied to 50k generated samples: **FID-Inception** [19] (InceptionV3 pool3, 2048-dim); **FD-DINOv3** [36] (CLS token of a large DINO-family ViT, 4096-dim); and **FD-VAE** [35] (SD-VAE latent scaled by 0.18215, 4096-dim), which measures distributional match in the generator’s native generation space \mathcal{M} . Offline post-hoc evaluation reports all three metrics at the best CFG weight w .

¹stabilityai/sd-vae-ft-mse on Hugging Face.

Latent SSL feature extractors. The matching geometry is determined by a frozen SSL feature extractor $\phi: \mathcal{M} \rightarrow \mathcal{F}$ applied directly to SD-VAE latents; all featurizers use a ViT backbone (32 layers, hidden dimension 1280, 16 heads, patch size 2) with attention-key facet feature extraction (Section C.1). We evaluate three families:

- **MAE (mask 50% / 60% / 75%).** ViT pretrained with masked autoencoding [18] directly on SD-VAE latents via token-level MSE reconstruction at three mask ratios (details in Section C.2.1).
- **DINOv3 distillation.** ViT student trained on SD-VAE latents to match the CLS and patch tokens of a frozen DINOv3 ViT-7B teacher [36] via cosine similarity loss (details in Section C.2.2).
- **Inception distillation.** ViT student trained on SD-VAE latents to match the features of a frozen InceptionV3 [19] (the same model used for FID) via cosine similarity loss (details in Section C.2.3).

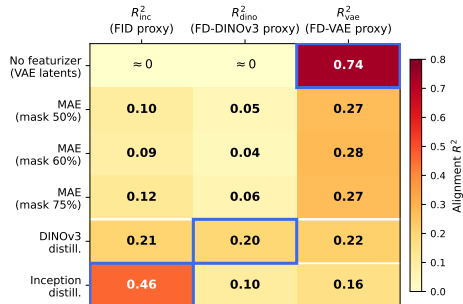


Figure 3: Featurizer–evaluation alignment R^2 for the six featurizers in Table 1. Each cell is the held-out R^2 of a linear map $\phi(x) \rightarrow \phi_*(x)$ fitted on 2048 ImageNet-256 latents (methodology in Section C.3). Higher values indicate smaller geometric misalignment (Δ^{geom}).

4.3 Results and Analysis

Table 1 reports generation quality and featurizer diagnostics for all families alongside the no-featurizer baseline.

The SSL featurizer is the primary lever. Without a featurizer, matching operates directly on VAE latent space ($\mathcal{M} = \mathcal{F}$): FID-Inception reaches 134.56. All SSL featurizers bring a dramatic improvement: FID-Inception drops to between 3.46 and 4.88 (27–39 \times), reflecting the fact that VAE features fail to produce semantically coherent transport couplings (Figure 2), while any SSL featurizer substantially sharpens class-level matching and sample quality (Figure 4). The choice of featurizer also matters: within the MAE family alone, FID-Inception varies from 6.66 (mask 75%) to 3.46 (mask 50%), a 1.9 \times spread from a single hyperparameter, and cross-family differences (3.46 vs. 4.88 for Inception distillation) are reflected in visible sample quality differences.

Geometric alignment alone does not determine generation quality. The alignment heatmap (Figure 3) reveals the expected self-alignment pattern: each featurizer aligns best with its own evaluation counterpart ($R^2_{\text{inc}} = 0.46$ for Inception distillation, $R^2_{\text{dino}} = 0.20$ for DINOv3 distillation, $R^2_{\text{vae}} = 0.74$ for the no-featurizer baseline). Yet across all three Fréchet metrics, the metric-matched featurizer is never the top performer: the best FID-Inception is MAE (3.46, not Inception distillation at 4.88), the best FD-DINOv3 is MAE (40.87, not DINOv3 distillation at 43.87), and the best FD-VAE is MAE (127.34, not the no-featurizer baseline at 179.80). Matching estimation accounts for this: the MAE family achieves lower effective rank (52.1–57.3 vs 68.0 for DINOv3 and 87.0 for Inception) and more stable transport targets ($\tilde{D}_{128} = 0.164\text{--}0.170$ vs 0.191 and 0.240), making its Sinkhorn training signal far more reliable per minibatch. Matching stability thus emerges as a key driver of generation performance across featurizer families. Single-cell RNA-seq experiments (Section E) further support this: within each generation space, \tilde{D}_{128} consistently predicts mean Fréchet rank across evaluation spaces, suggesting that matching stability is an important criterion for identifying which feature extractors will lead to successful generation.

Metric hacking: the Inception case. The Inception-distilled featurizer achieves FID-Inception = 4.88, better than MAE (mask 75%) at 6.66, yet Figure 4 shows its samples are substantially worse. The explanation lies in geometric alignment: with $R^2_{\text{inc}} = 0.46$ against the FID evaluation featurizer

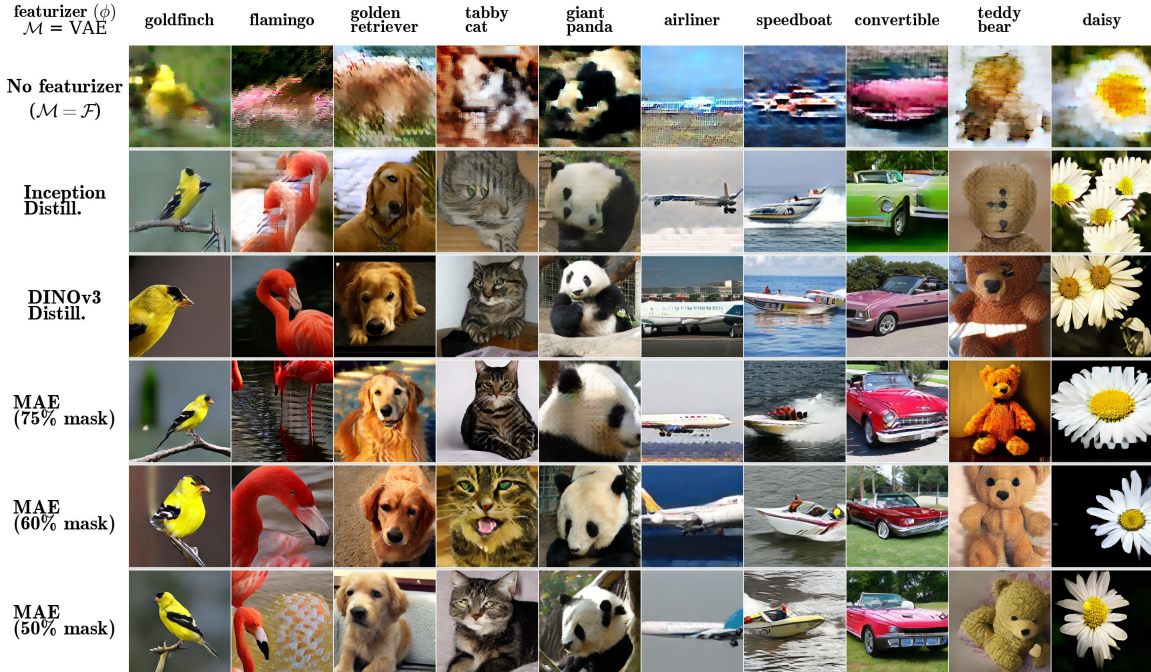


Figure 4: Uncurated class-conditional ImageNet samples from our method introduced in Section 3.2 (setup depicted in Figure 1). Each row corresponds to a different frozen SSL feature extractor ϕ used during training. Note that the SSL feature extractor is not used at test time.

(vs 0.12 for MAE mask 75%), the Inception featurizer shapes the generated distribution toward Inception features, improving the reported metric without improving perceptual quality. This is a concrete instance of metric hacking that FID alone cannot detect. We further quantify this effect in Section D, where we re-evaluate using the distilled featurizers directly in VAE latent space as evaluation featurizers: the Inception-distilled model achieves $\text{FD-Inc-d} = 0.17$ while simultaneously reaching $\text{FD-VAE} = 509$, confirming that zero geometric misalignment relative to one evaluation space can mask catastrophically poor generation in any other.

5 Conclusion

One-step generative models trained by distribution matching are principled approaches to generation. We show that lifting the matching objective to a semantically rich SSL feature space completely unlocks their potential, reducing FID-Inception by $39\times$ on class-conditional ImageNet. More importantly, we uncover the reasons: the mechanism is statistical, as semantic feature spaces have lower effective dimensionality, making matching estimation from finite minibatches reliable and matching stability a key criterion for feature extractor selection. We also find that using the evaluation featurizer for training reduces geometric misalignment but can make matching estimation harder, improving the reported score while degrading sample quality. This metric hacking effect is particularly striking with Inception, the reference featurizer used by the community for FID, reinforcing the need for evaluation criteria that go beyond a single fixed metric.

Our experiments use a DiT-B/2 generator, and scaling to larger architectures is a direct path to close the gap to the strongest one-step models [8]. A deeper open question is the trade-off between representational richness, which makes features broadly useful for downstream tasks, and the geometric compactness that enables stable matching estimation from finite minibatches; finding principled guidelines for navigating this balance is an important direction for future work.

References

- [1] Shir Amir, Yossi Gandelsman, Shai Bagon, and Tali Dekel. Deep vit features as dense visual descriptors. *arXiv preprint arXiv:2112.05814*, 2021. URL <https://arxiv.org/abs/2112.05814>.
- [2] Alma Andersson, Aya Abdelsalam Ismail, Edward De Brouwer, Doron Haviv, Tommaso Biancalani, Kyunghyun Cho, Gabriele Scalia, Aicha BenTaieb, and Hector Corrada Bravo. Single-cell concept bottleneck generative models for interpretable and controllable cellular editing. In *ICLR 2026 Workshop on Machine Learning for Genomics Explorations*, 2026.
- [3] Martin Arjovsky, Soumith Chintala, and Léon Bottou. Wasserstein generative adversarial networks. In *International Conference on Machine Learning*, pages 214–223. PMLR, 2017.
- [4] Randall Balestriero, Hugues Van Assel, Sami BuGhanem, and Lucas Maes. stable-pretraining-v1: Foundation model research made simple. *arXiv preprint arXiv:2511.19484*, 2025. URL <https://arxiv.org/abs/2511.19484>.
- [5] Tianci Bi, Xiaoyi Zhang, Yan Lu, and Nanning Zheng. Vision foundation models can be good tokenizers for latent diffusion models. *arXiv preprint arXiv:2510.18457*, 2025. URL <https://arxiv.org/abs/2510.18457>.
- [6] Bowei Chen, Sai Bi, Hao Tan, He Zhang, Tianyuan Zhang, Zhengqi Li, Yuanjun Xiong, Jianming Zhang, and Kai Zhang. AlignTok: Aligning Visual Foundation Encoders to Tokenizers for Diffusion Models. *arXiv preprint arXiv:2509.25162*, 2025. URL <https://arxiv.org/abs/2509.25162>.
- [7] Marco Cuturi. Sinkhorn distances: Lightspeed computation of optimal transport. In *Advances in Neural Information Processing Systems 26: 27th Annual Conference on Neural Information Processing Systems 2013*, pages 2292–2300, 2013. URL <https://proceedings.neurips.cc/paper/2013/hash/af21d0c97db2e27e13572cbf59eb343d-Abstract.html>.
- [8] Mingyang Deng, He Li, Tianhong Li, Yilun Du, and Kaiming He. Generative modeling via drifting. *arXiv preprint arXiv:2602.04770*, 2026.
- [9] Laurent Dinh, Jascha Sohl-Dickstein, and Samy Bengio. Density estimation using real NVP. In *5th International Conference on Learning Representations, ICLR 2017, Toulon, France, April 24-26, 2017, Conference Track Proceedings*. OpenReview.net, 2017. URL <https://openreview.net/forum?id=HkpbnH9lx>.
- [10] D. C. Dowson and B. V. Landau. The Fréchet distance between multivariate normal distributions. *Journal of Multivariate Analysis*, 12(3):450–455, 1982.
- [11] Jean Feydy, Thibault Séjourné, François-Xavier Vialard, Shun-ichi Amari, Alain Trounevé, and Gabriel Peyré. Interpolating between optimal transport and mmd using sinkhorn divergences. In *The 22nd international conference on artificial intelligence and statistics*, pages 2681–2690. PMLR, 2019.
- [12] Yuan Gao, Chen Chen, Tianrong Chen, and Jiatao Gu. One layer is enough: Adapting pretrained visual encoders for image generation. *arXiv preprint arXiv:2512.07829*, 2025. URL <https://arxiv.org/abs/2512.07829>.
- [13] Matthias Gelbrich. On a formula for the L^2 wasserstein metric between measures on euclidean and hilbert spaces. *Mathematische Nachrichten*, 147(1):185–203, 1990. doi: 10.1002/mana.19901470121.
- [14] Aude Genevay, Gabriel Peyré, and Marco Cuturi. Learning generative models with sinkhorn divergences. In *International Conference on Artificial Intelligence and Statistics*, pages 1608–1617. PMLR, 2018.

- [15] Ian J. Goodfellow, Jean Pouget-Abadie, Mehdi Mirza, Bing Xu, David Warde-Farley, Sherjil Ozair, Aaron C. Courville, and Yoshua Bengio. Generative adversarial nets. In *Advances in Neural Information Processing Systems 27: Annual Conference on Neural Information Processing Systems 2014, December 8-13 2014, Montreal, Quebec, Canada*, pages 2672–2680, 2014. URL <https://proceedings.neurips.cc/paper/2014/hash/5ca3e9b122f61f8f06494c97b1afccf3-Abstract.html>.
- [16] Jean-Bastien Grill, Florian Strub, Florent Althé, Corentin Tallec, Pierre H. Richemond, Elena Buchatskaya, Carl Doersch, Bernardo Ávila Pires, Zhaohan Guo, Mohammad Gheshlaghi Azar, Bilal Piot, Koray Kavukcuoglu, Rémi Munos, and Michal Valko. Bootstrap your own latent – A new approach to self-supervised learning. In *Advances in Neural Information Processing Systems 33 (NeurIPS 2020)*, 2020. URL <https://proceedings.neurips.cc/paper/2020/hash/f3ada80d5c4ee70142b17b8192b2958e-Abstract.html>.
- [17] Kaiming He, Haoqi Fan, Yuxin Wu, Saining Xie, and Ross Girshick. Momentum contrast for unsupervised visual representation learning. In *Proceedings of the IEEE/CVF conference on computer vision and pattern recognition*, pages 9726–9735, 2020.
- [18] Kaiming He, Xinlei Chen, Saining Xie, Yanghao Li, Piotr Dollár, and Ross B. Girshick. Masked autoencoders are scalable vision learners. In *IEEE/CVF Conference on Computer Vision and Pattern Recognition, CVPR 2022, New Orleans, LA, USA, June 18-24, 2022*, pages 15979–15988. IEEE, 2022. doi: 10.1109/CVPR52688.2022.01553. URL <https://doi.org/10.1109/CVPR52688.2022.01553>.
- [19] Martin Heusel, Hubert Ramsauer, Thomas Unterthiner, Bernhard Nessler, and Sepp Hochreiter. Gans trained by a two time-scale update rule converge to a local nash equilibrium. In I. Guyon, U. Von Luxburg, S. Bengio, H. Wallach, R. Fergus, S. Vishwanathan, and R. Garnett, editors, *Advances in Neural Information Processing Systems*, volume 30, pages 6626–6637. Curran Associates, Inc., 2017. URL https://proceedings.neurips.cc/paper_files/paper/2017/file/8a1d694707eb0fefe65871369074926d-Paper.pdf.
- [20] Jonathan Ho, Ajay Jain, and Pieter Abbeel. Denoising diffusion probabilistic models. In *Advances in Neural Information Processing Systems 33: Annual Conference on Neural Information Processing Systems 2020, NeurIPS 2020, December 6-12, 2020, virtual*, 2020. URL <https://proceedings.neurips.cc/paper/2020/hash/4c5bcfec8584af0d967f1ab10179ca4b-Abstract.html>.
- [21] Hyun Min Kang, Meena Subramaniam, Sasha Targ, Michelle Nguyen, Lenka Maliskova, Elizabeth McCarthy, Eunice Wan, Simon Wong, Lauren Byrnes, Cristina M Lanata, et al. Multiplexed droplet single-cell RNA-sequencing using natural genetic variation. *Nature Biotechnology*, 36(1): 89–94, 2018.
- [22] Diederik P. Kingma and Max Welling. Auto-encoding variational bayes. In *2nd International Conference on Learning Representations, ICLR 2014, Banff, AB, Canada, April 14-16, 2014, Conference Track Proceedings*, 2014. URL <http://arxiv.org/abs/1312.6114>.
- [23] Jiachen Lei, Keli Liu, Julius Berner, Haiming Yu, Hongkai Zheng, Jiahong Wu, and Xiangxiang Chu. There is no VAE: End-to-end pixel-space generative modeling via self-supervised pre-training. *arXiv preprint arXiv:2510.12586*, 2025. URL <https://arxiv.org/abs/2510.12586>.
- [24] Xingjian Leng, Jaskirat Singh, Yunzhong Hou, Zhenchang Xing, Saining Xie, and Liang Zheng. REPA-E: Unlocking VAE for End-to-End Tuning with Latent Diffusion Transformers. *arXiv preprint arXiv:2504.10483*, 2025. URL <https://arxiv.org/abs/2504.10483>.
- [25] Yujia Li, Kevin Swersky, and Rich Zemel. Generative moment matching networks. In *International Conference on Machine Learning*, pages 1718–1727. PMLR, 2015.

- [26] Yaron Lipman, Ricky T. Q. Chen, Heli Ben-Hamu, Maximilian Nickel, and Matthew Le. Flow matching for generative modeling. In *The Eleventh International Conference on Learning Representations, ICLR 2023, Kigali, Rwanda, May 1-5, 2023*. OpenReview.net, 2023. URL <https://openreview.net/forum?id=PqvMRDCJT9t>.
- [27] Xingchao Liu, Chengyue Gong, and Qiang Liu. Flow straight and fast: Learning to generate and transfer data with rectified flow. In *The Eleventh International Conference on Learning Representations, ICLR 2023, Kigali, Rwanda, May 1-5, 2023*. OpenReview.net, 2023. URL <https://openreview.net/forum?id=XVjTT1nw5z>.
- [28] Romain Lopez, Jeffrey Regier, Michael B Cole, Michael I Jordan, and Nir Yosef. Deep generative modeling for single-cell transcriptomics. *Nature Methods*, 15(12):1053–1058, 2018.
- [29] Ilya Loshchilov and Frank Hutter. Decoupled weight decay regularization. In *7th International Conference on Learning Representations, ICLR 2019*. OpenReview.net, 2019. URL <https://openreview.net/forum?id=Bkg6RiCqY7>.
- [30] Maxime Oquab, Timothée Darcet, Théo Moutakanni, Huy V. Vo, Marc Szafraniec, Vasil Khalidov, Pierre Fernandez, Daniel Haziza, Francisco Massa, Alaaeldin El-Nouby, Mido Assran, Nicolas Ballas, Wojciech Galuba, Russell Howes, Po-Yao Huang, Shang-Wen Li, Ishan Misra, Michael Rabbat, Vasu Sharma, Gabriel Synnaeve, Hu Xu, Hervé Jégou, Julien Mairal, Patrick Labatut, Armand Joulin, and Piotr Bojanowski. DINOv2: Learning robust visual features without supervision. *Transactions on Machine Learning Research*, 2024. URL <https://openreview.net/forum?id=a68SUt6zFt>.
- [31] William Peebles and Saining Xie. Scalable diffusion models with transformers. In *Proceedings of the IEEE/CVF International Conference on Computer Vision*, pages 4172–4182, 2023.
- [32] Gabriel Peyré and Marco Cuturi. Computational optimal transport. *Foundations and Trends in Machine Learning*, 11(5-6):355–607, 2019. doi: 10.1561/22000000073. URL <https://doi.org/10.1561/22000000073>.
- [33] Aram-Alexandre Pooladian and Jonathan Niles-Weed. Entropic estimation of optimal transport maps. *arXiv preprint arXiv:2109.12004*, 2021. URL <https://arxiv.org/abs/2109.12004>.
- [34] Martin Rohbeck, Edward De Brouwer, Charlotte Bunne, Jan-Christian Huetter, Anne Biton, Kelvin Chen, Aviv Regev, and Romain Lopez. Modeling complex system dynamics with flow matching across time and conditions. In *International Conference on Learning Representations*, volume 2025, pages 12164–12188, 2025.
- [35] Robin Rombach, Andreas Blattmann, Dominik Lorenz, Patrick Esser, and Björn Ommer. High-resolution image synthesis with latent diffusion models. *arXiv preprint arXiv:2112.10752*, 2022. URL <https://arxiv.org/abs/2112.10752>.
- [36] Oriane Siméoni, Huy V. Vo, Maximilian Seitzer, Federico Baldassarre, Maxime Oquab, Cijo Jose, Vasil Khalidov, Marc Szafraniec, Seungeun Yi, Michaël Ramamonjisoa, Francisco Massa, Daniel Haziza, Luca Wehrstedt, Jianyuan Wang, Timothée Darcet, Théo Moutakanni, Leonel Sentana, Claire Roberts, Andrea Vedaldi, Jamie Tolan, John Brandt, Camille Couprie, Julien Mairal, Hervé Jégou, Patrick Labatut, and Piotr Bojanowski. DINOv3. *arXiv preprint arXiv:2508.10104*, 2025. URL <https://arxiv.org/abs/2508.10104>.
- [37] Jaskirat Singh, Xingjian Leng, Zongze Wu, Liang Zheng, Richard Zhang, Eli Shechtman, and Saining Xie. What matters for representation alignment: Global information or spatial structure? *arXiv preprint arXiv:2512.10794*, 2025. URL <https://arxiv.org/abs/2512.10794>.
- [38] Yang Song, Jascha Sohl-Dickstein, Diederik P. Kingma, Abhishek Kumar, Stefano Ermon, and Ben Poole. Score-based generative modeling through stochastic differential equations. In *9th International Conference on Learning Representations, ICLR 2021, Virtual Event, Austria, May 3-7, 2021*. OpenReview.net, 2021. URL <https://openreview.net/forum?id=PxTIG12RRHS>.

- [39] Christian Szegedy, Vincent Vanhoucke, Sergey Ioffe, Jon Shlens, and Zbigniew Wojna. Rethinking the inception architecture for computer vision. In *2016 IEEE Conference on Computer Vision and Pattern Recognition (CVPR)*, pages 2818–2826. IEEE Computer Society, 2016. URL <https://doi.org/10.1109/CVPR.2016.308>.
- [40] Hugues Van Assel, Mark Ibrahim, Tommaso Biancalani, Aviv Regev, and Randall Balestriero. Joint embedding vs reconstruction: Provable Benefits of Latent Space Prediction for Self Supervised Learning. In *Advances in Neural Information Processing Systems*, 2025. URL <https://arxiv.org/abs/2505.12477>.
- [41] Cédric Villani. *Optimal Transport: Old and New*, volume 338. Springer Science & Business Media, 2008. doi: 10.1007/978-3-540-71050-9.
- [42] Runqian Wang and Kaiming He. Diffuse and Disperse: Image Generation with Representation Regularization. *arXiv preprint arXiv:2506.09027*, 2025. URL <https://arxiv.org/abs/2506.09027>.
- [43] Ziqiao Wang, Wangbo Zhao, Yuhao Zhou, Zekai Li, Zhiyuan Liang, Mingjia Shi, Xuanlei Zhao, Pengfei Zhou, Kaipeng Zhang, Zhangyang Wang, Kai Wang, and Yang You. REPA works until it doesn't: Early-stopped, holistic alignment supercharges diffusion training. *arXiv preprint arXiv:2505.16792*, 2025. URL <https://arxiv.org/abs/2505.16792>.
- [44] Jingfeng Yao, Bin Yang, and Xinggang Wang. Reconstruction vs. generation: Taming optimization dilemma in latent diffusion models. In *IEEE/CVF Conference on Computer Vision and Pattern Recognition, CVPR 2025, Nashville, TN, USA, June 11-15, 2025*, pages 15703–15712. Computer Vision Foundation / IEEE, 2025. doi: 10.1109/CVPR52734.2025.01464. URL https://openaccess.thecvf.com/content/CVPR2025/html/Yao_Reconstruction_vs._Generation_Taming_Optimization_Dilemma_in_Latent_Diffusion_Models_CVPR_2025_paper.html.
- [45] Sihyun Yu, Sangkyung Kwak, Huiwon Jang, Jongheon Jeong, Jonathan Huang, Jinwoo Shin, and Saining Xie. Representation Alignment for Generation: Training Diffusion Transformers Is Easier Than You Think. *arXiv preprint arXiv:2410.06940*, 2024. URL <https://arxiv.org/abs/2410.06940>.
- [46] Boyang Zheng, Nanye Ma, Shengbang Tong, and Saining Xie. Diffusion Transformers with Representation Autoencoders. *arXiv preprint arXiv:2510.11690*, 2025. URL <https://arxiv.org/abs/2510.11690>.

Table of Contents

- **Section A: Notation.** Summary of symbols used in the main text.
- **Section B: Sinkhorn Algorithms and Gradient.** Log-domain Sinkhorn iterations, symmetric Sinkhorn for self-transport, and the particle gradient of the Sinkhorn divergence.
- **Section C: Implementation Details.** Full training pipeline, feature extraction, normalization, and hyperparameters.
- **Section D: Latent-Space Evaluation with Distilled Featurizers.** Evaluation using the training featurizer directly as ϕ_* , eliminating geometric misalignment by construction and isolating matching estimation as the sole driver of generation quality.
- **Section E: Single-Cell RNA-Seq Generation.** Extended setup, diagnostics, and qualitative results for the single-cell domain.
- **Section F: Drifting and Sinkhorn Divergence: Detailed Comparison.** Precise relationship between the drifting objective and the Sinkhorn divergence gradient, including theoretical grounding and performance comparison.

A Notation

We collect here only the notation reused across multiple sections. Symbols used only locally are introduced where they first appear.

Setup (Section 3.1).

- \mathcal{X} : ambient data space; p : data distribution on \mathcal{X} .
- \mathcal{M} : generation space; p_0 : prior on \mathcal{M} .
- $g_\theta: \mathcal{M} \rightarrow \mathcal{M}$: one-step generator; Enc: $\mathcal{X} \rightarrow \mathcal{M}$: encoder; Dec: $\mathcal{M} \rightarrow \mathcal{X}$: decoder.
- \mathcal{F} : training feature space; $\phi: \mathcal{M} \rightarrow \mathcal{F}$: frozen SSL feature extractor.
- \mathcal{F}_* : evaluation feature space; $\phi_*: \mathcal{M} \rightarrow \mathcal{F}_*$: evaluation featurizer.

Measures, objectives, and transport maps (Sections 2, 3.1 and 3.2).

- $q_{\phi,g} = (\phi \circ g) \# p_0$, $r_\phi = (\phi \circ \text{Enc}) \# p$: generated and real feature marginals in training space.
- $q_{*,g} = (\phi_* \circ g) \# p_0$, $r_* = (\phi_* \circ \text{Enc}) \# p$: generated and real feature marginals in evaluation space.
- $\hat{q}_{\phi,g} = \frac{1}{N} \sum_i \delta_{\phi(g(\mathbf{u}_{0,i}))}$, $\hat{r}_\phi = \frac{1}{N} \sum_j \delta_{\phi(\text{Enc}(\mathbf{x}_j))}$: empirical feature measures.
- $\text{OT}_\varepsilon(\alpha, \beta)$, $S_\varepsilon(\alpha, \beta)$: entropic OT cost and Sinkhorn divergence for generic discrete measures α , β on \mathcal{F} .
- $J_\phi(g) := W_2^2(q_{\phi,g}, r_\phi)$, $J_*(g) := W_2^2(q_{*,g}, r_*)$: population Wasserstein objectives.
- $\hat{J}_{\phi,\varepsilon,N}(g) := S_\varepsilon(\hat{q}_{\phi,g}, \hat{r}_\phi)$: empirical Sinkhorn objective.
- $\Delta_\phi^{\text{geom}}(g) := |J_*(g) - J_\phi(g)|$: geometric misalignment.
- $\Delta_{\phi,\varepsilon,N}^{\text{est}}(g) := |J_\phi(g) - \hat{J}_{\phi,\varepsilon,N}(g)|$: transport-estimation gap.

- $q_{\phi, \theta}(\cdot|c, w) := (\phi \circ g_{\theta}(\cdot|c, w))_{\#} p_0$, $r_{\phi}^c := (\phi \circ \text{Enc})_{\#} p(\cdot|c)$, $r_{\phi}^u := (\phi \circ \text{Enc})_{\#} p$: generated, conditional-real, and unconditional-real feature distributions for CFG.
- $w \geq 0$: classifier-free guidance weight.
- $\pi^{q,r}, \pi^{q,q}$: optimal cross- and self-couplings.
- $\hat{T}_{\varepsilon}^{q,r}(\mathbf{h}_i) := N \sum_j \pi_{ij}^{q,r} \mathbf{h}_j^r$, $\hat{T}_{\varepsilon}^{q,q}(\mathbf{h}_i) := N \sum_k \pi_{ik}^{q,q} \mathbf{h}_k$: cross- and self-barycentric projections.
- $\hat{T}_{\varepsilon}^{q,c}$, $\hat{T}_{\varepsilon}^{q,u}$: conditional and unconditional cross-transport barycenters in the CFG objective.
- $\hat{T}_{\varepsilon}^{\text{cfg}}$: guided barycentric field from equation 14.

Evaluation metrics (Section 4.1).

- $\text{FD}_{\phi_{\star}}$: Fréchet distance in evaluation feature space \mathcal{F}_{\star} .
- \tilde{D}_N : OT matching-estimation stability metric.

B Sinkhorn Algorithms and Gradient

This appendix provides the log-domain algorithms for computing OT_{ε} and the particle gradient of the Sinkhorn divergence used in training. Entropic OT and the Sinkhorn divergence are defined in Section 2; for full derivations see [7, 32, 11].

Sinkhorn iterations. The dual potentials $\mathbf{f}, \mathbf{g} \in \mathbb{R}^N$ solving $\text{OT}_{\varepsilon}(\alpha, \beta)$ satisfy the fixed-point conditions

$$f_i = \varepsilon \log(1/N) + \min_{\varepsilon}(C_{i.} - \mathbf{g}), \quad (17)$$

$$g_j = \varepsilon \log(1/N) + \min_{\varepsilon}(C_{.j} - \mathbf{f}), \quad (18)$$

where $\min_{\varepsilon}(\mathbf{S})_i := -\varepsilon \log \sum_j \exp(-S_{ij}/\varepsilon)$ is the soft-minimum operator (converging to $\min_j S_{ij}$ as $\varepsilon \rightarrow 0$). Starting from $\mathbf{f} = \mathbf{g} = \mathbf{0}$, alternating these updates is the Sinkhorn algorithm [7]. Algorithm 1 gives the complete log-domain procedure.

Algorithm 1 Sinkhorn algorithm (log-domain)

Require: Cost matrix $\mathbf{C} \in \mathbb{R}^{N \times N}$, regularization $\varepsilon > 0$, iterations K

- 1: $f \leftarrow \mathbf{0} \in \mathbb{R}^N$, $g \leftarrow \mathbf{0} \in \mathbb{R}^N$
 - 2: **for** $\ell = 1, \dots, K$ **do**
 - 3: $f_i \leftarrow \varepsilon \log(1/N) + \min_{\varepsilon}(C_{i.} - \mathbf{g})$ for each i \triangleright Update \mathbf{f}
 - 4: $g_j \leftarrow \varepsilon \log(1/N) + \min_{\varepsilon}(C_{.j} - \mathbf{f})$ for each j \triangleright Update \mathbf{g}
 - 5: **end for**
 - 6: $\pi \leftarrow \frac{1}{N^2} \exp((\mathbf{f} \oplus \mathbf{g} - \mathbf{C})/\varepsilon)$ \triangleright Recover optimal coupling
 - 7: **return** π
-

In our setting, $C_{ij} = \|\mathbf{h}_i - \mathbf{h}'_j\|^2$ for cross-transport and the returned coupling is $\pi^{q,r}$; for self-transport use Algorithm 2.

Symmetric Sinkhorn for self-transport. For the self-transport problem $\text{OT}_{\varepsilon}(\alpha, \alpha)$, the dual problem is symmetric: $\mathbf{f} = \mathbf{g}$ at optimality. The optimal potential can therefore be found by a single *symmetric* damped fixed-point update [11]:

$$f_i \leftarrow \frac{1}{2}(f_i + \varepsilon \log N + \min_{\varepsilon}(C_{i.} - \mathbf{f})) \quad \text{for each } i,$$

Algorithm 2 Symmetric Sinkhorn algorithm (log-domain)

Require: Symmetric cost matrix $\mathbf{C} \in \mathbb{R}^{N \times N}$, regularization $\varepsilon > 0$, iterations K

- 1: $f \leftarrow \mathbf{0} \in \mathbb{R}^N$
 - 2: **for** $\ell = 1, \dots, K$ **do**
 - 3: $f_i \leftarrow \frac{1}{2}(f_i + \varepsilon \log N + \min_\varepsilon(\mathbf{C}_{i \cdot} - \mathbf{f}))$ for each i \triangleright *Symmetric update*
 - 4: **end for**
 - 5: $\boldsymbol{\pi} \leftarrow \frac{1}{N^2} \exp((\mathbf{f} \oplus \mathbf{f} - \mathbf{C})/\varepsilon)$ \triangleright *Recover symmetric coupling*
 - 6: **return** $\boldsymbol{\pi}$
-

which converges significantly faster than the standard alternating scheme: in practice 3–5 iterations suffice. Algorithm 2 gives the complete procedure.

In our setting, $C_{ij} = \|\mathbf{h}_i - \mathbf{h}_j\|^2$ for self-transport and the returned coupling is $\boldsymbol{\pi}^{q,q}$.

Particle gradient of S_ε . The gradient of S_ε with respect to generated features recovers the entropic barycentric estimator of [33], linking the practical Sinkhorn update directly to the matching estimation theory of Section 2. By the envelope theorem, treating the couplings as fixed at their optimal values [11]:

$$\begin{aligned} \nabla_{\mathbf{h}_i} S_\varepsilon(\alpha, \beta) &= \nabla_{\mathbf{h}_i} \text{OT}_\varepsilon(\alpha, \beta) - \frac{1}{2} \nabla_{\mathbf{h}_i} \text{OT}_\varepsilon(\alpha, \alpha) \\ &= 2 \sum_j \pi_{ij}^{\alpha, \beta} (\mathbf{h}_i - \mathbf{h}'_j) - \frac{1}{2} \left[2 \sum_k \pi_{ik}^{\alpha, \alpha} (\mathbf{h}_i - \mathbf{h}_k) + 2 \sum_k \pi_{ki}^{\alpha, \alpha} (\mathbf{h}_i - \mathbf{h}_k) \right] \\ &= 2 \sum_j \pi_{ij}^{\alpha, \beta} (\mathbf{h}_i - \mathbf{h}'_j) - 2 \sum_k \pi_{ik}^{\alpha, \alpha} (\mathbf{h}_i - \mathbf{h}_k), \end{aligned} \tag{19}$$

where $\boldsymbol{\pi}^{\alpha, \beta}$ and $\boldsymbol{\pi}^{\alpha, \alpha}$ are the optimal couplings for $\text{OT}_\varepsilon(\alpha, \beta)$ and $\text{OT}_\varepsilon(\alpha, \alpha)$ respectively ($\text{OT}_\varepsilon(\beta, \beta)$ is free of $\{\mathbf{h}_i\}$), and the last step uses $\pi_{ik}^{\alpha, \alpha} = \pi_{ki}^{\alpha, \alpha}$. Equivalently, in our setting, $\nabla_{\mathbf{h}_i} S_\varepsilon = -\frac{2}{N} (\hat{T}_\varepsilon^{q,r}(\mathbf{h}_i) - \hat{T}_\varepsilon^{q,q}(\mathbf{h}_i))$, recovering equation 12. The cross-transport term $\hat{T}_\varepsilon^{q,r}$ is the entropic barycentric estimator of [33]: its convergence to the population Monge map at rate equation 4 is what makes the intrinsic dimensionality d the key quantity controlling matching estimation quality per minibatch. The self-transport term $\hat{T}_\varepsilon^{q,q}$ is the debiasing correction inherited from the Sinkhorn divergence.

C Implementation Details

This section provides the training details and hyperparameters for the generator (Section C.1), the SSL feature extractor training procedures (Section C.2), and the encoder–evaluation alignment methodology (Section C.3). All experiments were run on NVIDIA B200 GPUs and are implemented on top of the `stable-pretraining-v1` framework [4], which provides the training loop, checkpointing, and configuration infrastructure.

C.1 Generator Training

This subsection details the training procedure for the one-step generator g_θ .

Training loop. Each training step samples N_c classes, generates N_{neg} samples per class, draws N_{pos} class-matched real targets and N_{unc} unconditional real targets, and associates each class with a guidance weight w_c . Each training step proceeds as follows:

1. Sample a batch of N_c class labels and per-class guidance weights w_c .
2. For each class c : generate N_{neg} images, draw N_{pos} positives and N_{unc} unconditional samples from queues.
3. Extract multi-scale features on all generated, positive, and unconditional samples.

4. Normalize features; compute the conditional cross-, unconditional cross-, and self-transport targets; normalize.
5. Compute the Sinkhorn divergence loss summed over all classes and features.
6. Run backpropagation and update parameters; update EMA.

The remainder of this section elaborates on each component.

Data loading, queues, and batching. At each training step, N_c class labels are sampled uniformly at random and N_{neg} images are generated per class, yielding an effective batch size $B = N_c \times N_{\text{neg}}$. Real samples are provided by a standard DataLoader and used only to populate two CPU-resident queues [17]: a *per-class* queue of size $Q_c = 128$ for positive samples and a *global* unconditional queue of size $Q_u = 1000$ for CFG negatives. At each step, N_{pos} positive samples are drawn from the class-matched queue and N_{unc} unconditional samples from the global queue.

Multi-scale feature extraction via attention keys. To capture feature structure at multiple levels of abstraction, we extract features from several intermediate layers of the ViT backbone rather than relying on the final block output alone. At each tapped layer we use *attention key vectors* [1] rather than block output tokens: key vectors are computed before self-attention aggregation and MLP mixing, and therefore retain finer spatial structure than the corresponding block outputs.

For the backbone described in Section C.2 (depth 32), we tap every 8 layers (layers 8, 16, 24, 32). At each tapped layer, we apply `norm1` (the pre-attention layer norm), project through the QKV linear layer, select the key slice, apply `k_norm` (key normalization from QK-norm, if present), and reshape into a spatial map of shape (B, C, H_p, W_p) , where $H_p = W_p = 16$ for 32×32 SD-VAE latents with patch size 2 and $C = 1280$ (see Section C.2). From each spatial map we form three feature blocks:

- **per_loc**: the $H_p W_p = 256$ spatial key vectors, shape $(B, 256, C)$;
- **global_mean**: their mean-pooled vector, shape $(B, 1, C)$;
- **global_std**: their std-pooled vector, shape $(B, 1, C)$.

This yields $4 \times 3 = 12$ named blocks. Each spatial position within a block defines an independent OT sub-problem [8]: for a **per_loc** block with 256 positions, there are 256 independent Sinkhorn problems, each matching N -sample empirical measures in \mathbb{R}^C ; the two global blocks each contribute one sub-problem in \mathbb{R}^C . In total, a ViT-H encoder produces $4 \times (256 + 1 + 1) + 1 = 1033$ independent OT sub-problems per class (the final +1 is the input-norm feature: the per-channel spatial RMS of the input VAE latent, a vector in \mathbb{R}^4 that contributes one additional OT sub-problem). Per-location matching provides spatially resolved gradient signal: each position independently constrains the generator to produce correct local content at that grid location. Scalar featurizer diagnostics (effective rank, \bar{D}_N) are aggregated across sub-problems by a weighted average, with weight equal to the number of spatial positions in the block (256 for **per_loc**, 1 for global blocks), so the reported value is dominated by the per-location sub-problems.

Each feature type ϕ_j is normalized independently so that pairwise distances are of order 1 regardless of feature dimension, ensuring that the Sinkhorn regularization ε controls the entropy–fidelity tradeoff consistently across all sub-problems. The normalization scale is

$$S_j = \frac{\text{scale}_j}{\sqrt{C_j}},$$

where $C_j = C$ is the feature dimension and scale_j is computed with stop-gradient as the empirical mean L_2 distance from generated features to the full target pool $[\phi_j(\mathbf{x}_{\text{gen}}), \phi_j(\mathbf{x}_{\text{unc}}), \phi_j(\mathbf{x}_{\text{pos}})]$, concatenated across all spatial positions within the block [8]. The Sinkhorn regularization strength is then set data-adaptively: $\tilde{\varepsilon} = \tau \cdot \text{std}(\mathbf{C}^{q,r})$, where $\text{std}(\mathbf{C}^{q,r})$ is the empirical standard deviation of the cross-transport cost matrix entries (computed after feature normalization), making the base temperatures $\tau \in \{0.02, 0.05, 0.2\}$ scale-invariant.

OT barycenter normalization. After computing $\hat{T}_\varepsilon^{\text{cfg}}$ (defined in equation 14) for each (ϕ_j, ε) pair, the normalization scale is

$$\lambda_j = \sqrt{\mathbb{E}\left[\frac{1}{C_j} \|\hat{T}_\varepsilon^{\text{cfg}}(\mathbf{h}_i)\|^2\right]},$$

and the normalized transport target is $\tilde{T}_j = \hat{T}_\varepsilon^{\text{cfg}}/\lambda_j$. We use three regularization values $\varepsilon \in \{0.02, 0.05, 0.2\}$: for each ε , $\tilde{T}_{j,\varepsilon}$ is computed and normalized independently, and the aggregated target is $\tilde{T}_j = \sum_\varepsilon \tilde{T}_{j,\varepsilon}$. All normalization statistics are computed with stop-gradient. Features at different spatial locations within the same feature map share a single normalization scale, computed by concatenating all locations.

Classifier-free guidance. CFG is implemented via the Sinkhorn CFG objective equation 13. For each class c , three Sinkhorn problems are solved: the conditional cross-transport between $q_{\phi,\theta}(\cdot|c, w_c)$ and r_ϕ^c , the unconditional cross-transport between $q_{\phi,\theta}(\cdot|c, w_c)$ and r_ϕ^u , and the self-transport of $q_{\phi,\theta}(\cdot|c, w_c)$. They are combined into $\hat{T}_\varepsilon^{\text{cfg}}$ equation 14 with guidance weight $w_c \geq 0$. Following [8], the self-transport cost matrix has its diagonal set to $+\infty$ ($C_{ii}^{q,q} = +\infty$, see Section F) to prevent trivial self-matching, and is solved via the symmetric Sinkhorn algorithm (Algorithm 2). The self-transport solve is shared across both Sinkhorn divergences. The N_{unc} unconditional real samples drawn per class from the global queue serve as the target for the unconditional cross-transport solve. At each training step, w_c is sampled from the power-law distribution $p(w) \propto w^{-\kappa}$ on $[w_{\min}, w_{\max}]$ via inverse-CDF sampling, and the generator is conditioned on (c, w_c) via adaptive layer normalization (adaLN) [31]. At inference, a single forward pass with a user-specified w produces the output; no Sinkhorn computation is needed at test time.

Optimizer and EMA. The total loss $\mathcal{L} = \sum_j \mathcal{L}_j$ sums over feature types after averaging each term over its class-location entries. We use AdamW [29] with $(\beta_1, \beta_2) = (0.9, 0.95)$, gradient clipping at norm 2.0, and a linear warmup followed by linear decay schedule. An EMA copy of the generator with decay 0.999 is updated after each step.

C.2 SSL Feature Extractor Training

This subsection details the training procedures for the SSL feature extractors used to define the matching cost during generator training.

Featurizer architecture. All featurizers share the same transformer backbone: hidden dimension 1280, depth 32, 16 attention heads, SwiGLU MLP (hidden dim 5120), RMSNorm, and RMSNorm applied to queries and keys before attention (QK-norm), operating on SD-VAE latents of shape $32 \times 32 \times 4$ (scaled by 0.18215) with patch size 2, yielding 256 tokens. This common capacity and input format ensures that differences in generation quality and OT diagnostics across featurizer families reflect differences in SSL training objective rather than model size or input representation.

Training setup. All featurizers are trained with AdamW ($\beta_1 = 0.9$, $\beta_2 = 0.95$, weight decay 0.05) in bf16 mixed precision, with an EMA copy (decay 0.9995) used for checkpointing. Input images undergo pixel-space augmentation (RandomResizedCrop at 256×256 , RandomHorizontalFlip) followed by on-the-fly SD-VAE encoding with posterior sampling.

We now describe the training objective specific to each featurizer family.

C.2.1 MAE Featurizer Pretraining

Each MAE feature extractor is pretrained from scratch with masked autoencoding directly on SD-VAE latents.

Decoder architecture. The decoder uses hidden dimension 512, depth 4, and 16 heads.

Pretraining. Masking operates at the token level (after patch embedding): a fraction m of the 256 tokens is randomly removed before the encoder ($m \in \{50\%, 60\%, 75\%\}$), and the decoder predicts the original latent patches for all masked positions. The loss is MSE restricted to masked positions. Training uses learning rate 1.5×10^{-4} with 10k-step linear warmup and global batch size 4096, running for 1280 epochs (≈ 400 k steps).

Classification fine-tuning. For all three mask variants, we append 3000 additional steps with a combined loss $\mathcal{L} = (1 - \lambda)\mathcal{L}_{\text{recon}} + \lambda\mathcal{L}_{\text{cls}}$, where λ is linearly warmed from 0 to 0.1 over the first 1000 steps. \mathcal{L}_{cls} is the cross-entropy loss of a linear head (1280 \rightarrow 1000) applied to the encoder CLS token. This step adds a weak semantic signal without discarding the reconstruction geometry.

C.2.2 DINOv3 Distillation

The DINOv3-distilled featurizer trains a student with the architecture described above on SD-VAE latents to match the features of a frozen DINOv3 ViT-7B teacher operating on pixels.

Distillation. Two linear projection heads map student features to the teacher dimension: a global head (1280 \rightarrow 4096) applied to the CLS token and a patch head (1280 \rightarrow 4096) applied to all 256 patch tokens. The teacher is a frozen DINOv3 ViT-7B-16 pretrained on pixels [36]; it receives 256×256 pixel crops (scale $[0.4, 1.0]$, to avoid tiny crops that degrade patch-token supervision) and produces a 4096-dim CLS token and 256 patch tokens. The student receives the corresponding SD-VAE latents and produces its own CLS and patch tokens. Both sides are L2-normalized before computing cosine similarity losses on CLS ($\lambda_{\text{cls}} = 0.1$) and patch tokens ($\lambda_{\text{patch}} = 1.0$). Training uses learning rate 10^{-4} with 5k-step linear warmup and global batch size 2048, for 200 epochs (≈ 125 k steps).

C.2.3 Inception Distillation

The Inception-distilled featurizer trains a student with the architecture described above on SD-VAE latents to match the pool3 features of a frozen InceptionV3 network (the same model used for FID computation [19]).

Distillation. A single linear projection head (1280 \rightarrow 2048) maps the mean-pooled student tokens to the Inception feature space. The teacher is a frozen InceptionV3 [39], receiving 256×256 pixel crops (scale $[0.4, 1.0]$, converted to uint8 $[0, 255]$) and producing 2048-dim pool3 features. The student receives the corresponding SD-VAE latents and produces a global descriptor by mean-pooling its 256 patch tokens. Both sides are L2-normalized before computing the cosine similarity loss between the projected student features and the teacher pool3 features. Training uses the same schedule as DINOv3 distillation: learning rate 10^{-4} with 5k-step linear warmup and global batch size 2048, for 200 epochs (≈ 125 k steps).

C.3 Featurizer–Evaluation Alignment

The geometric misalignment term $\Delta_{\phi}^{\text{geom}}$ in the bound equation 11 is the key quantity linking the training featurizer ϕ to the evaluation metric: when ϕ and ϕ_{\star} induce similar matching geometries, improving the Sinkhorn training objective translates into gains on the evaluation metric; when they diverge, the two objectives partially decouple. Computing $\Delta_{\phi}^{\text{geom}}(g_{\theta}) = |J_{\star}(g_{\theta}) - J_{\phi}(g_{\theta})|$ directly requires a trained generator, making it a post-hoc diagnostic rather than a tool for featurizer selection. We instead measure a featurizer-level proxy: the held-out R^2 of a linear map $A: \mathcal{F} \rightarrow \mathcal{F}_{\star}$ fitting $A\phi(\mathbf{x}) \approx \phi_{\star}(\mathbf{x})$, which is computable before any generation training and captures whether ϕ_{\star} 's geometry is linearly recoverable from ϕ .

The R^2 is fitted via kernel ridge regression on 2048 ImageNet-256 latents ($\lambda = 0.1$, features L2-normalised per sample before fitting). $R^2 \approx 1$ means ϕ already contains ϕ_{\star} 's information linearly (small geometric misalignment); $R^2 \approx 0$ means the two featurizers live in unrelated spaces. Three

evaluation featurizers are used: InceptionV3 pool3 (2048-dim), DINOv3 ViT-7B CLS token (4096-dim), and the SD-VAE flat latent scaled by 0.18215 (4096-dim). The resulting R^2 heatmap for the six ViT-H featurizers and its interpretation are in Figure 3 and the surrounding discussion in Section 4.2.

D Latent-Space Evaluation with Distilled Featurizers

Table 1 evaluates in pixel-space feature spaces (InceptionV3, DINOv3 ViT-7B) that differ from the distilled latent-space featurizers used during training. To isolate the effect of geometric alignment, Table 2 evaluates the same generators using these distilled latent-space featurizers directly as ϕ_* . By construction, this sets $\Delta_\phi^{\text{geom}} = 0$ (Equation (11)), leaving matching estimation as the sole driver of the training-evaluation gap and providing a controlled test of its relative importance.

When the training featurizer matches the evaluation featurizer, FD drops sharply: Inception-distilled training achieves FD-Inc-d = 0.17, and DINOv3-distilled training achieves FD-DINOv3-d = 3.03, both far below any cross-featurizer evaluation. However, the Inception-distilled model that scores 0.17 in its own feature space simultaneously achieves FD-VAE = 509, the worst latent-space reconstruction of any featurizer, confirming that near-perfect self-alignment is an artifact of matching the evaluation geometry rather than a sign of generation quality. The MAE 50% featurizer achieves the best FD-MAE50 (1.76) and, notably, the best FD-Inc-d (0.08), outperforming the Inception-distilled featurizer even in the latter’s own matched evaluation space, confirming that matching estimation quality is an independent driver of generation performance, strong enough to compensate for geometric misalignment.

Table 2: Latent-space Fréchet distance: evaluation with distilled featurizers applied directly to VAE latents. Each column uses a different latent-space featurizer as ϕ_* . **Shading** : training featurizer ϕ matches the evaluation featurizer.

Featurizer	FD-VAE↓	FD-DINOv3-d↓	FD-Inc-d↓	FD-MAE50↓
No featurizer ($\mathcal{M} = \mathcal{F}$)	179.93	156.59	4.49	125.58
Inception distill.	508.77	13.91	0.17	10.31
DINOv3 distill.	100.26	3.03	0.09	1.74
MAE (mask 75%)	126.01	5.80	0.17	2.68
MAE (mask 50%)	126.82	5.45	0.08	1.76

E Single-Cell RNA-Seq Generation

Setup. We apply our method to cell-type-conditional single-cell RNA-seq generation on a standard scRNA-seq stimulation dataset [21] (16,839 cell profiles, 3,000 genes after standard preprocessing). The generator g_θ is a 6-layer MLP mapping Gaussian noise to the generation space \mathcal{M} , conditioned on cell-type labels via one-hot concatenation. Three representation spaces are considered: *ambient* (\mathbb{R}^{3000} , the log-normalized gene expression vector), *PCA* (\mathbb{R}^{128} , the top principal components of the ambient space, a commonly used single cell representation in generative models [34, 2]), and *scVI* (\mathbb{R}^{30} , the latent embedding of a pretrained variational autoencoder for single-cell data [28]). We compare six configurations that vary the generation space \mathcal{M} and the Sinkhorn coupling space ϕ : **PCA / scVI** ($\mathcal{M} = \mathbb{R}_{\text{PCA}}^{128}$, $\phi = \text{scVI}$), **ambient / scVI** ($\mathcal{M} = \mathbb{R}^{3000}$, $\phi = \text{scVI}$), **PCA / PCA** ($\mathcal{M} = \mathbb{R}_{\text{PCA}}^{128}$, $\phi = \text{Id}$), **ambient / ambient** ($\mathcal{M} = \mathbb{R}^{3000}$, $\phi = \text{Id}$), **ambient / PCA** ($\mathcal{M} = \mathbb{R}^{3000}$, $\phi = \text{PCA}$), and **scVI / scVI** ($\mathcal{M} = \mathbb{R}_{\text{scVI}}^{30}$, $\phi = \text{Id}$). Generation quality is measured by conditional and unconditional Fréchet distances in three evaluation spaces: the 30-dimensional scVI latent, the 128-dimensional PCA space, and the 3000-dimensional ambient expression space. Each configuration is run over 5 seeds.

Table 3: Single-cell generation results (Kang dataset, cell-type-conditional, test set). Fréchet distances computed in three evaluation spaces. Effective rank and \tilde{D}_{128} characterize the coupling embedding space. Mean \pm SEM over 5 seeds. **Bold**: best per column; underline: second best; **shading**: training featurizer ϕ matches the evaluation featurizer (diagonal entries).

Config (\mathcal{M} / ϕ)	Cond. FD _{scVI} ↓	FD _{scVI} ↓	Cond. FD _{PCA} ↓	FD _{PCA} ↓	Cond. FD _{amb} ↓	FD _{amb} ↓	Eff. rank	\tilde{D}_{128} ↓
PCA / PCA	2.28 \pm 0.01	1.26 \pm 0.02	22.84 \pm 0.22	15.71 \pm 0.03	93.16 \pm 0.22	78.08 \pm 0.03	20.0	0.54
PCA / scVI	1.77 \pm 0.04	0.78 \pm 0.03	24.91 \pm 0.15	<u>17.41</u> \pm 0.08	95.20 \pm 0.15	79.69 \pm 0.07	16.3	<u>0.89</u>
ambient / PCA	2.51 \pm 0.02	1.50 \pm 0.01	<u>24.43</u> \pm 0.44	<u>17.80</u> \pm 0.03	<u>94.13</u> \pm 0.45	78.64 \pm 0.05	20.0	0.54
ambient / ambient	2.55 \pm 0.03	1.51 \pm 0.02	24.90 \pm 0.58	17.82 \pm 0.04	<u>94.62</u> \pm 0.58	78.60 \pm 0.04	260.8	0.91
ambient / scVI	<u>1.81</u> \pm 0.02	<u>0.90</u> \pm 0.03	26.72 \pm 0.24	19.37 \pm 0.09	96.05 \pm 0.24	79.58 \pm 0.08	16.3	<u>0.89</u>
scVI / scVI	3.02 \pm 0.02	2.24 \pm 0.01	50.47 \pm 0.09	36.62 \pm 0.05	124.21 \pm 0.11	101.14 \pm 0.06	16.3	<u>0.89</u>

Table 4: Mean rank across all twelve Fréchet distance metrics in Table 3 (3 evaluation spaces \times conditional/unconditional \times val/test). Lower \tilde{D}_{128} of the coupling space consistently predicts lower (better) mean FD rank within a given generation space, mirroring the ImageNet finding (Section 4).

Config (\mathcal{M} / ϕ)	\tilde{D}_{128} ↓	Eff. rank	Mean FD rank↓
PCA / PCA	0.54	20.0	1.67
PCA / scVI	0.89	16.3	2.83
ambient / PCA	0.54	20.0	3.00
ambient / ambient	0.91	260.8	3.67
ambient / scVI	0.89	16.3	3.83
scVI / scVI	0.89	16.3	6.00

Results. Table 3 reports generation quality alongside coupling-space diagnostics, and Table 4 aggregates these into a mean rank across all twelve Fréchet distance metrics. As in the image setting, the OT stability metric \tilde{D}_{128} is predictive of generation quality. Within a given generation space, the coupling with lowest \tilde{D}_{128} consistently achieves the best mean FD rank. Among PCA-space generators, PCA coupling ($\tilde{D}_{128} = 0.54$) ranks first (1.67) while scVI coupling ($\tilde{D}_{128} = 0.89$) ranks 2.83. Among ambient-space generators, PCA coupling again leads (rank 3.00), ahead of ambient ($\tilde{D}_{128} = 0.91$, rank 3.67) and scVI coupling (rank 3.83). Generating directly in the scVI latent (scVI/scVI) is consistently worst, as the 30-dimensional generation space is too restrictive for the generator to express a sufficiently rich transport map. Figure 5 confirms this visually: PCA/PCA and PCA/scVI closely reproduce the reference cluster geometry, whereas scVI/scVI collapses several cell-type populations.

Conclusion. Table 4 shows that OT stability is predictive of which feature space leads to best generation in general. PCA shows the lowest \tilde{D}_{128} and boasts the best performance across the different model spaces (PCA and ambient). While the effective rank appears less predictive of performance in this case, the difference between PCA (20) and scVI (16.3) is marginal. Finally, we note that while scVI is a viable choice of feature space, using it as a model space severely degrades performance, which we attribute to the poor performance of the scVI decoder. This highlights an important strength of our approach: leveraging a model space where reconstruction is highly accurate (but OT stability may be low) and a feature space where OT stability is high (but reconstruction may be poor).

F Drifting and Sinkhorn Divergence: Detailed Comparison

Drifting [8] is a recent one-step generative model that, like our method, uses frozen SSL features to define a transport objective in latent space. This appendix spells out the drifting construction and explains its precise relationship to the Sinkhorn divergence.

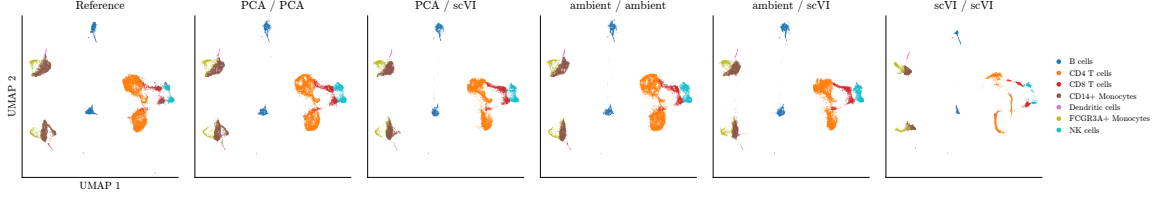


Figure 5: UMAP visualization of reference and generated cells for six configurations, colored by cell type. PCA / PCA and PCA / scVI closely reproduce the reference cluster geometry, while scVI / scVI collapses several populations.

Construction. Let $\mathbf{h}_i = \phi(\mathbf{u}_i)$ for $i = 1, \dots, N$ be feature vectors of N generated samples and $\mathbf{h}_j^r = \phi(\mathbf{u}_j^r)$ for $j = 1, \dots, M$ be feature vectors of M real samples. Define the pairwise squared-Euclidean costs

$$C_{ij}^{q,r} = \|\mathbf{h}_i - \mathbf{h}_j^r\|^2, \quad C_{ik}^{q,q} = \|\mathbf{h}_i - \mathbf{h}_k\|^2, \quad C_{ii}^{q,q} = +\infty, \quad (20)$$

where the diagonal mask eliminates self-interactions. These are concatenated column-wise into a single cost matrix $\bar{C} \in \mathbb{R}^{N \times (M+N)}$, pooling real and generated samples as joint targets.

Drifting then applies a symmetric row/column softmax normalization on \bar{C} at temperature $\tau > 0$:

$$A_{it} := \sqrt{\frac{\exp(-\bar{C}_{it}/\tau)}{\sum_s \exp(-\bar{C}_{is}/\tau)} \cdot \frac{\exp(-\bar{C}_{it}/\tau)}{\sum_\ell \exp(-\bar{C}_{\ell t}/\tau)}}, \quad (21)$$

so A_{it} is the geometric mean of a row-wise and a column-wise softmax: a weight is large only when the pair is cheap both within its source row and within its target column.

Splitting A into real and generated blocks $A^+ \in \mathbb{R}^{N \times M}$ and $A^- \in \mathbb{R}^{N \times N}$, the rows of each block are rescaled so that each particle i contributes equal total mass to attraction and repulsion:

$$W_{ij}^+ = \frac{A_{ij}^+}{\sum_j A_{ij}^+}, \quad W_{ik}^- = \frac{A_{ik}^-}{\sum_k A_{ik}^-}.$$

The resulting drifting field is

$$\mathbf{v}_i = \sum_j W_{ij}^+ \mathbf{h}_j^r - \sum_{k \neq i} W_{ik}^- \mathbf{h}_k,$$

and the model is trained by regressing \mathbf{h}_i toward $\text{sg}[\mathbf{h}_i + \mathbf{v}_i]$, where $\text{sg}[\cdot]$ denotes stop-gradient.

Relation to Sinkhorn divergence. The double-softmax in equation 21 is built from the same Gibbs kernel $\exp(-C/\tau)$ as entropic OT: each row softmax normalizes over source particles and each column softmax over target particles, so A_{it} approximates a coupling density. Splitting A into a cross block A^+ (generated vs. real) and a self block A^- (generated vs. generated) then mirrors the attraction–repulsion structure of the Sinkhorn divergence gradient: A^+ attracts generated particles toward real data and A^- pushes them apart, replicating the cross- and self-transport terms of ∇S_ε .

Two key differences separate drifting from the Sinkhorn divergence gradient:

- **One step vs. convergence.** The double-softmax in equation 21 amounts to a single iteration of Sinkhorn-Knopp: one round of row normalization and one of column normalization applied simultaneously. A single step does not produce a doubly stochastic coupling: A satisfies neither its prescribed row marginals nor its column marginals, so mass is not properly allocated to each source or target particle. Our method iterates two independent Sinkhorn solves until both marginal constraints are jointly satisfied, yielding properly normalized couplings (Section B).
- **Coupled vs. decoupled transports.** Drifting normalizes a single concatenated cost matrix, so the attraction block A^+ and the repulsion block A^- share the same marginal budget. Our

method solves two entirely separate problems (one for $q_{\phi,\theta}$ against r_ϕ and one for $q_{\phi,\theta}$ against itself), so attraction and repulsion carry independent marginal constraints and cannot interfere with each other.

- **Theoretical grounding.** The Sinkhorn divergence is a theoretically principled objective: it interpolates between the Wasserstein distance and the MMD [11], and its population limit is directly linked to the W_2 distance that underlies Fréchet-style evaluation metrics. This connection is what motivates using it as a training objective for generation quality measured by FID and related scores (Section 4.1). The drifting objective, by contrast, lacks this theoretical interpretation: the double-softmax normalization and cross-scaling do not correspond to the gradient of any known population-level divergence, making it difficult to reason about what the model optimizes at convergence.

Performance comparison and scaling. Our Sinkhorn-based method with a DiT-B/2 generator achieves FID-Inception 3.46 (Table 1), close to the 3.36 reported by [8] at the same generator scale. Direct comparison is limited, however, for two reasons. First, our SSL featurizers use a ViT backbone trained with our own recipes (Sections C.2.1 to C.2.3), while drifting uses a ResNet featurizer; the backbone architecture and training procedure materially shape the transport geometry and generation quality, making the feature extractors non-interchangeable. Second, as the metric hacking analysis in Section 4 shows, FID is sensitive to the choice of training featurizer: a featurizer well-aligned to Inception features can improve the reported score while degrading actual sample quality, so FID alone is an unreliable basis for cross-method comparison when featurizers differ. Scaling the generator from DiT-B/2 to DiT-L/2, as drifting demonstrates, remains a direct path toward competitive generation performance.

G Additional Generated Samples

We provide additional uncurated class-conditional ImageNet samples across 30 diverse classes, complementing the 10 classes shown in Figure 4. Each figure follows the same layout: rows correspond to different frozen SSL feature extractors used during training, and columns correspond to ImageNet classes. All samples are generated in one step and decoded by the frozen SD-VAE decoder; the SSL feature extractor is not used at inference.

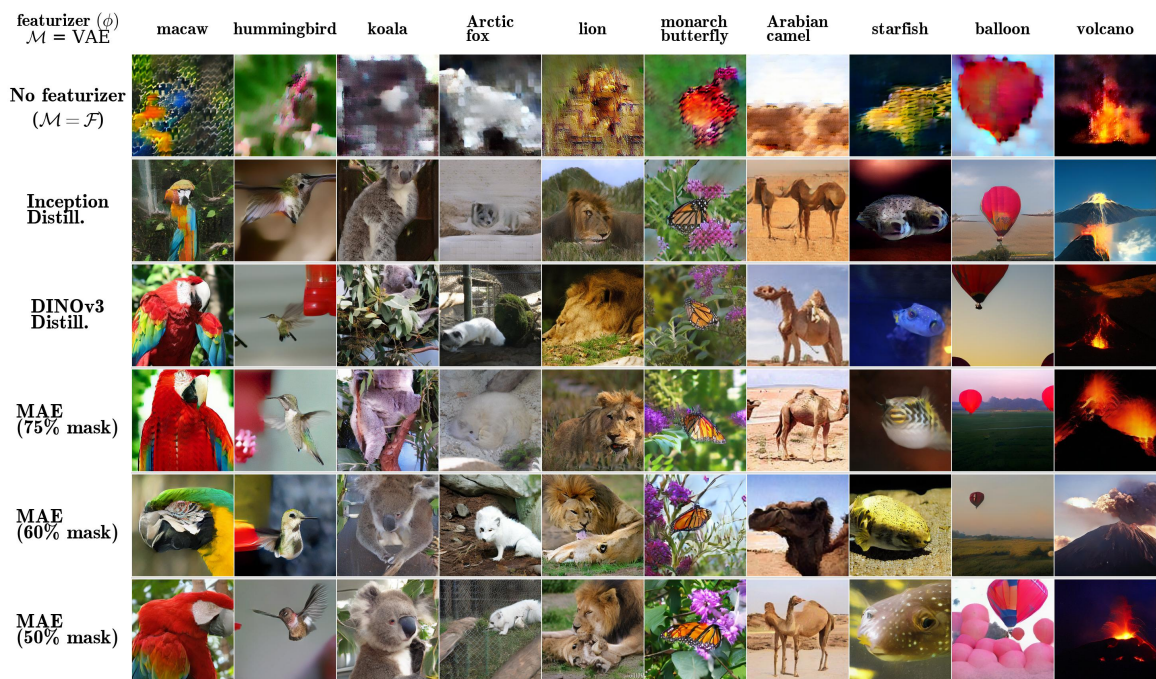


Figure 6: Additional uncurated samples (classes: macaw, hummingbird, koala, Arctic fox, lion, monarch butterfly, Arabian camel, starfish, balloon, volcano). Same setup as Figure 4.

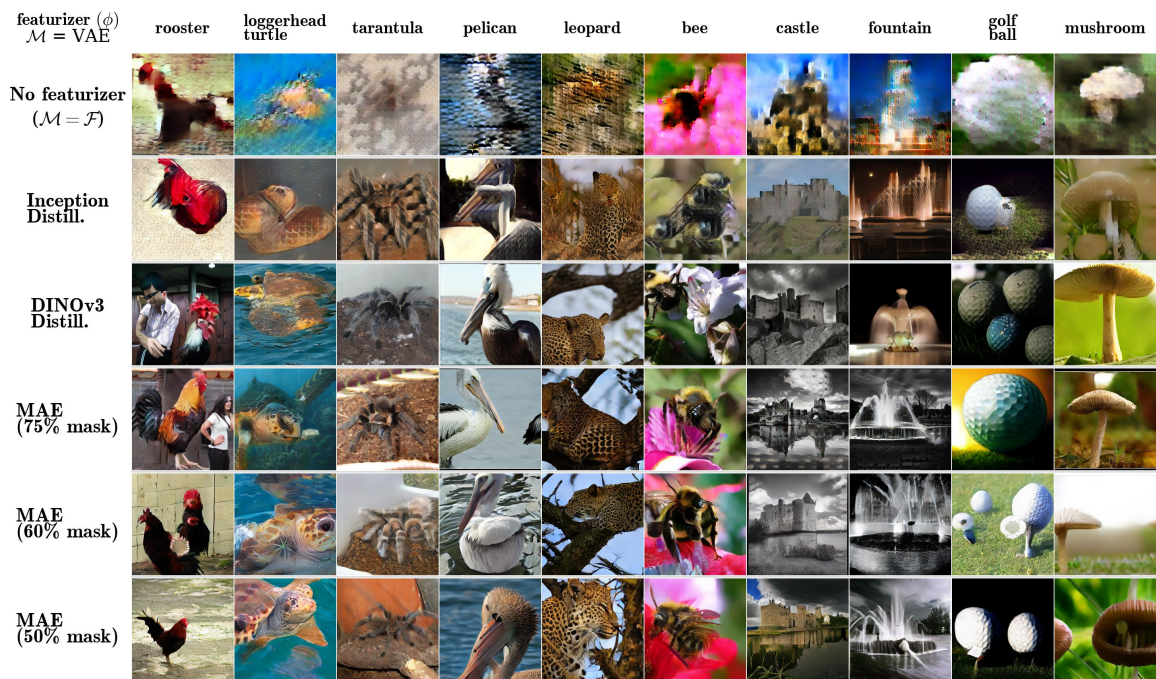


Figure 7: Additional uncurated samples (classes: rooster, loggerhead turtle, tarantula, pelican, leopard, bee, castle, fountain, golf ball, mushroom). Same setup as Figure 4.

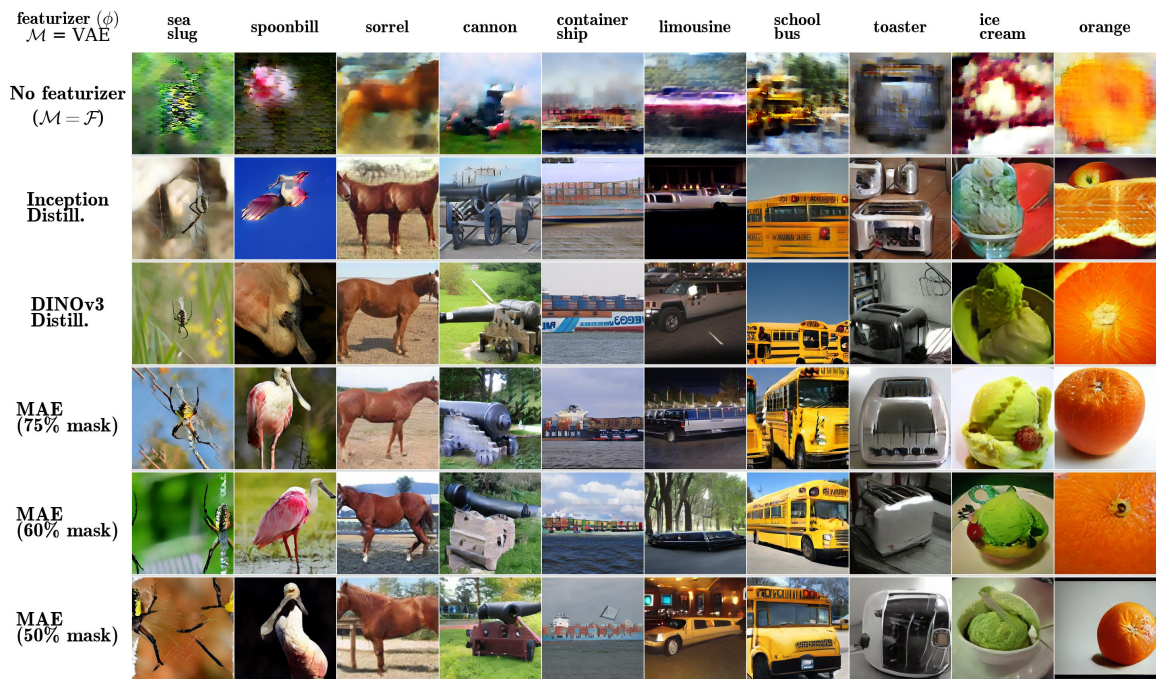


Figure 8: Additional uncurated samples (classes: sea slug, spoonbill, sorrel, cannon, container ship, limousine, school bus, toaster, ice cream, orange). Same setup as Figure 4.